

Magnetized CMB observables: a dedicated numerical approach

Massimo Giovannini^{a,c} and Kerstin E. Kunze^{b,c}

^a*Centro “Enrico Fermi”, Compendio del Viminale, Via Panisperna 89/A, 00184 Rome, Italy*

^b*Departamento de Física Fundamental,
Universidad de Salamanca, Plaza de la Merced s/n, E-37008 Salamanca, Spain*

^c*Department of Physics, Theory Division, CERN, 1211 Geneva 23, Switzerland*

Abstract

Large-scale magnetic fields affect the scalar modes of the geometry whose ultimate effect is to determine the anisotropies of the Cosmic Microwave Background (CMB in what follows). For the first time, a consistent numerical approach to the magnetized CMB anisotropies is pursued with the aim of assessing the angular power spectra of temperature and polarization when the scalar modes of the geometry and a stochastic background of inhomogeneous magnetic fields are simultaneously present in the plasma. The effects related to the magnetized nature of the plasma are taken into account both at the level of the dynamical equations and at the level of the initial conditions of the Einstein-Boltzmann hierarchy. The temperature and polarization observables are exploited to infer the peculiar signatures of a pre-equality magnetic field. Using the extrapolated best fit to the three year WMAP data the increase and distortions of the first seven peaks in the TT autocorrelations are monitored for different values of the regularized magnetic field intensity and for the physical range of spectral indices. Similar analyses are also conducted for the first few anticorrelation (and correlation) peaks of the TE power spectra. Possible interesting degeneracies and stimulating perspectives are pointed out and explored.

1 The general framework

The origin of large-scale magnetic fields is still a poorly understood subject as much as the origin of the primordial spectrum of the density contrast was unclear almost two score years ago when the first attempts of understanding the origin of large-scale structure actually begun. The first observational evidence of the existence of large-scale magnetic fields in our galaxy goes back to the work of Hiltner [1] and Hall [2] (see also [3]). The problem, in itself, has many facets which can be summarized as follows:

- observational evidence of the existence of large-scale magnetic fields is indisputable from a number of different observations ranging from Faraday rotation to synchrotron emission;
- objects of different sizes (and different evolutionary histories) possess sizable magnetic fields in the μ G range: a striking example of this statement are, for instance, spiral galaxies, elliptical galaxies and a class of x-ray bright Abell clusters;
- theoretical evidence of the mechanism responsible of the degree of magnetization of the present Universe is still under active discussion.

We have a rather plausible control of the dynamics of electromagnetic fields in plasmas: since the pioneering work of Alfvén [4] the various descriptions of weakly coupled plasmas have been tested both in astrophysical systems and, most importantly, laboratory experiments [5, 6, 7, 8]. Various plasma descriptions (covering different branches of the spectrum of plasma excitations) allow to predict instabilities in terrestrial tokamaks. An example of successful (but not unique) framework is the one-fluid plasma theory which, under some circumstances, reduces to the well known magnetohydrodynamics (MHD in what follows). All the astrophysical attempts for the justification of large scale magnetic fields rest on the assumption that, at some time prior to galaxy formation, appropriate initial conditions for the MHD evolution should be present. While this point of view is shared by the whole community, opinions vary as far as the real primordial nature of magnetic fields is concerned. For informative reviews on this broad subject the interested reader may usefully consult the publications reported in [9] (see also [10] for more observational aspects of large-scale magnetization).

Theoretical diatribes cannot decide whether or not large-scale magnetic fields are a cosmic relic. It is more rewarding, in our opinion, to apply Occam's razor and pose a more modest but yet experimentally answerable question: were large-scale magnetic fields present prior to matter-radiation equality? The latter question is answerable since, as it will be specifically shown, the effects of large-scale magnetic fields can be read-off from the properties of CMB observables.

In recent years diverse data sets seem to conspire towards a sort of paradigm which is customarily employed in the interpretation of cosmological data. This paradigm is often dubbed as Λ CDM lore where Λ stands for the dark-energy component (parametrized as a cosmological constant) and CDM stands for the cold dark matter component. The data sets supporting this general view range from the CMB data¹ to the large-scale structure data [17, 18] and, finally, to the type Ia supernova data in their various incarnations [19, 20] (see also [21] for weak lensing data). The combined analysis of these three classes of data support the Λ CDM paradigm. A primordial spectrum of adiabatic perturbations,

¹ Among them, the WMAP data [11, 12, 13, 14, 15], the data of other balloon borne experiments as well as the data of various terrestrial arrays [16].

present for typical wavelengths larger than the Hubble radius prior to Hydrogen recombination and after matter-radiation equality, is the main responsible for the normalization of the CMB temperature autocorrelations (TT correlations in what follows). The cross-correlations between temperature and polarization (TE correlations in what follows) lead to a typical anticorrelation peak [14] which is often quoted as the golden signature of the predominant adiabaticity of the CMB initial conditions. The polarization autocorrelations (EE correlations in what follows) have been partially observed by the WMAP experiment itself [12] as well as by other terrestrial arrays. The viability of the Λ CDM paradigm is customarily completed by the addition of various parameters whose explicit determination can either confirm or improve the pure Λ CDM scenario. Among these models we can mention, just as an example, the addition of a tensor component, the inclusion of a specific form of the barotropic index for the dark energy component (different from the one of a pure cosmological constant), the search for specific corrections in the scalar power spectrum motivated, with various degrees of theoretical accuracy, by the (yet unknown) physics of the Planck energy scale (see, for instance, some of the analyses reported in [11]). There is the hope that the unprecedented accuracy of the data of the Planck explorer mission [22] will allow to rule in (or rule out) some of these theoretical possibilities ².

The aim of this paper is to complement the Λ CDM paradigm with the presence of a pre-decoupling magnetic field (see also [25]). Such a completion is not only motivated theoretically but also observationally: since we do observe large-scale magnetic fields later on, it is plausible to posit, as falsifiable hypothesis, their existence also prior to equality. Definite answers to such a question will come, in this context, by confronting the completion of the Λ CDM paradigm with all the available cosmological data in the same way as, for instance, a pristine tensor contribution to the CMB anisotropies can be constrained by adding, in the parameter estimation, a stochastic background of long-wavelength gravitons. In this investigation one of the first goals of the program will be reached: a dedicated numerical approach for the magnetized CMB observables will be constructed. Without this step sound strategies of parameter estimation will be forlorn. This step is often rather straightforward in different cases since all the available codes contemplate, for instance, the inclusion of tensor modes or the inclusion of a peculiar barotropic index for the dark energy component. However the latter statement does not apply to the case of large-scale magnetic fields.

The analysis of the interplay between large-scale magnetic fields and CMB observables might be traced back to the pioneering works of Zeldovich [26] and Harrison [27]. In recent years it has been understood that large-scale magnetic fields may affect the vector and tensor modes of the geometry and may also affect, indirectly, the CMB polarization [28, 29] (see, for instance, [30] for a topical review on this subject). The main obstacle to a systematic analysis of the current data in the light of a magnetized component is represented by our lack of understanding of the close relationship between the large-scale magnetic fields and the *scalar* modes of the geometry. Indeed, as explicitly suggested by observations, the inhomogeneities in the CMB temperature and polarization can be attributed to curvature perturbations.

An impasse then seems to arise. The vector and tensor modes induced by large-scale magnetic fields are very small at large length scales (i.e. small multipoles). It is thus rather hard to imagine the possibility of including the magnetic field contribution as an appropriate fit parameter in an extended version of the Λ CDM paradigm if the effects of magnetic fields on the scalar modes of the geometry are unknown.

²Various models going beyond the pure Λ CDM scenario can be confronted with the foreseeable sensitivities of the high and low frequency instruments embarked on the Planck spacecraft. See, for instance, [23, 24].

A theoretical framework for the analysis of scalar modes of the geometry and large-scale magnetic fields has been recently developed in a series of papers ranging from the accurate determinations of adiabatic initial conditions in the presence of a scalar mode of the geometry [31], to the extension of the tight-coupling expansion [32] and to the semi-analytical calculation of temperature autocorrelations [33]. One of the aims of the present paper is to translate into a dedicated numerical approach all the theoretical understanding of the interplay between the scalar modes of the geometry and the large scale magnetic fields that has been pursued, through various steps, in [31, 32, 33]. The CMB effects related to the scalar modes of the geometry are the most difficult ones already in the absence of large-scale magnetic fields. The complication comes from the physical observation that the density contrasts of the various species do not couple to the tensor and the vector modes but they do couple to the scalar modes of the geometry. Conversely the curvature perturbations are the source of the evolution of the density contrasts for photons, for baryons and for the CDM species. In the magnetized case this occurrence is even more acute since large-scale magnetic fields and plasma effects propagate both at the level of the Boltzmann hierarchy and at the level of the perturbed Einstein equations.

The approach studied in the present investigation is based on a faithful MHD description of the pre-decoupling plasma. More refined descriptions of the high frequency branch of the spectrum of plasma excitations (valid for frequencies comparable with the electron plasma frequency) must reproduce anyway the approach described here when the typical length-scales and dynamical times are, respectively, much larger than the Debye length and much larger than the inverse of the plasma frequency [5, 6].

The plasma will not only be populated by an electromagnetic component but also by fluctuations of the geometry which should be treated relativistically since their typical wavelengths, at the onset of the numerical calculation, will be much larger than the Hubble radius at the corresponding epoch. The description of the scalar modes of the geometry will be formulated in the peculiar language of the synchronous coordinate system. One of the first codes developed for the analysis of CMB anisotropies is COSMICS [34, 35]. The CMBFAST [36, 37] code is based originally on COSMICS and in many respects it can be said that COSMICS is the ancestor of CMBFAST. As in COSMICS, also in CMBFAST the dynamical evolution across equality and decoupling is followed in the synchronous coordinate system. The synchronous approach carries necessarily a possible ambiguity on the complete removal of the gauge freedom. It is actually known since the early eighties [38] that, in the synchronous gauge, the coordinate system is only fixed up to a pair of space-dependent integration constants. The remaining gauge freedom must be removed from the initial conditions of the Boltzmann hierarchy to avoid the dangerous presence of spurious (i.e. gauge) modes. The way to handle this potentially annoying problem resides in the ability of treating the same problem also in contiguous gauges where the gauge parameters are completely fixed. An example of this technique is the longitudinal gauge [27, 35, 39] (see also [40]) which has been also exploited for this purpose in the absence of magnetic fields. This will also be the path followed in the present analysis (see also [31, 32]) by including consistently the effects due to the global magnetization of the plasma. Finally, in the present study the scalar vector and tensor modes are separated on the basis of their transformation properties under three-dimensional rotations [39] (see also [41]). There exist approaches which are fully covariant [42] and which have been also applied to the case of large-scale magnetic fields [43] without leading, however, to any explicit estimate either of the Sachs-Wolfe plateau or of the temperature autocorrelations in the Doppler region as reported in [31].

With these specifications in mind, our code is based on CMBFAST with integration along the line of sight. The main difference stems from the consistent introduction of a magnetized component

both at the level of the initial conditions and at the level of the dynamical equations. This choice has been also dictated by the fact that the WMAP collaboration used also CMBFAST for the analysis of the observational data. It is plausible to think that this numerical approach can be also effective throughout the next decade for the analysis of forthcoming data like the ones of the Planck explorer [22].

The plan of our paper is therefore the following. In Section 2 we will review the main evolution equations to be integrated. Particular attention will be given to the way large-scale magnetic fields are included in the pre-equality and pre-decoupling physics. In Section 3 a theory of the magnetized initial conditions will be formulated when the dominant source of curvature inhomogeneities is the standard adiabatic mode. Section 4 is devoted to the calculation of temperature autocorrelations. The results on the polarization observables are collected in Section 5. The distinctive features introduced in the angular power spectra by the presence of large-scale magnetic fields will be further scrutinized in Section 6. Section 7 contains our concluding remarks. In the Appendix we collected auxiliary material on the longitudinal gauge description sticking, however, only to those themes that are germane to our calculations.

2 The full content of the magnetized plasma

Below the temperature of neutrino decoupling, the content of the plasma is formed both by neutral species and charged species. The neutral species are cold dark matter (CDM in what follows), neutrinos (which will be taken to be massless) and photons. The charged species are baryons and electrons. The three observational data sets (i.e. CMB anisotropies [11, 12], large-scale structure [17, 18] and type Ia supernovae [19, 20]) suggest, that a cosmological constant term should also be added. The pivotal Λ CDM lore is then delicately improved by positing, already prior to equality, that the primeval plasma is effectively magnetized.

Neutral species are indirectly affected by the presence of large-scale magnetic fields. In fact, magnetic fields gravitate and contribute both to the Hamiltonian and momentum constraints as well as to the dynamical evolution of the gravitational inhomogeneities. The evolution of the charged species will be followed using MHD [5, 6, 8] generalized to the situation where the geometry is dynamical and where gravitational inhomogeneities are also simultaneously present. The adoption of this scheme is dictated by the typical hierarchy of the Coulomb and Thompson scatterings.

The position of the first Doppler peak implies, in a Λ CDM framework, that the background geometry is spatially flat. The inclusion of spatial curvature amounts to an overall shift of the TT power spectra and hence to a change in the position of the first peak. The line element can then be written, in the conformal time coordinate τ , as:

$$ds^2 = a^2(\tau)[d\tau^2 - d\vec{x}^2], \quad a(\tau)d\tau = dt, \quad \mathcal{H} = \frac{a'}{a} = aH. \quad (2.1)$$

In Eq. (2.1), t denotes the cosmic time coordinate and H the Hubble rate; the prime will denote, throughout the paper, a derivation with respect to the conformal time coordinate τ . The evolution of the scale factor $a(\tau)$ is determined by the appropriate Friedmann-Lemaître equations:

$$\mathcal{H}^2 = \frac{8\pi G}{3} a^2 \rho_t, \quad (2.2)$$

$$\mathcal{H}^2 - \mathcal{H}' = 4\pi G a^2 (p_t + \rho_t), \quad (2.3)$$

$$\rho_t' + 3\mathcal{H}(\rho_t + p_t) = 0, \quad (2.4)$$

where ρ_t and p_t denote, respectively, the total energy density and pressure of the plasma, i.e.

$$\rho_t = \rho_c + \rho_\nu + \rho_\gamma + \rho_e + \rho_b + \rho_\Lambda, \quad p_t = \frac{\rho_\nu}{3} + \frac{\rho_\gamma}{3} - \rho_\Lambda. \quad (2.5)$$

The subscripts in Eq. (2.5) refer to the various components of the plasma mentioned in the first paragraph of the current section.

The time scales involved in the present study are the ones encountered in CMB physics: the equality time (at which the radiation and the matter component have equal weight in Eq. (2.2)), the recombination time (at which the ionization fraction drops because neutral Hydrogen is formed), the decoupling time (at which the mean free path of the photons becomes comparable with the Hubble radius). The exact solution of Eqs. (2.2), (2.3) and (2.4) in the absence of dark energy component (which can be neglected around decoupling) stipulates that the scale factor interpolates, in the conformal time coordinate τ , between a linear evolution (typical of the pre-equality plasma) and a quadratic evolution (typical of the plasma around recombination and decoupling):

$$a(\tau) = a_{\text{eq}} \left[\left(\frac{\tau}{\tau_1} \right)^2 + 2 \left(\frac{\tau}{\tau_1} \right) \right], \quad \tau_1 = \frac{2}{H_0} \sqrt{\frac{a_{\text{eq}}}{\Omega_{\text{M}0}}} \simeq 288.15 \left(\frac{\omega_{\text{M}}}{0.134} \right)^{-1} \text{Mpc}. \quad (2.6)$$

In Eq. (2.6) $\omega_{\text{M}} = h_0^2 \Omega_{\text{M}0}$ where h_0 (of the order of 0.7 in the standard Λ CDM framework) is the current indetermination on the Hubble rate. Given a generic species X , $\omega_X = h_0^2 \Omega_{X0}$: while Ω_{X0} is proportional to h_0^{-2} , ω_X is, by its definition, independent of h_0 (this is the reason why it is sometimes called Hubble-free critical fraction). To estimate τ_1 in Eq. (2.6) it has been used that $\omega_\gamma = 2.47 \times 10^{-5}$, $\omega_\nu = 1.68 \times 10^{-5}$ and $\omega_{\text{R}} = \omega_\nu + \omega_\gamma = 4.15 \times 10^{-5}$. In the code Eqs. (2.2), (2.3) and (2.4) are integrated numerically. Equation (2.6) can be anyway used for semi-analytical estimates [32] and for the important problem of correctly setting the initial conditions of the Einstein-Boltzmann hierarchy (see Section 3). According to Eq. (2.6) $\tau_{\text{eq}} = (\sqrt{2} - 1)\tau_1 \simeq \tau_1/2$. The redshift is defined as $1 + z = a_0/a$ by fixing $a_0 = 1$. The recombination redshift (taken for instance between 1050 and 1100) will determine, via Eq. (2.6) τ_{rec} (note that $\tau_{\text{rec}} > \tau_{\text{eq}}$).

The coupled evolution of the fluctuations of the geometry (2.1) with the fluctuations of the plasma quantities will determine, thanks to the interaction with the magnetic fields, the peculiar features of the magnetized CMB anisotropies. The synchronous coordinate system is most easily presented already in Fourier space and it can be written as³

$$\delta_s g_{ij}(k, \tau) = a^2(\tau) \left[\hat{k}_i \hat{k}_j h(k, \tau) + 6\xi(k, \tau) \left(\hat{k}_i \hat{k}_j - \frac{1}{3} \delta_{ij} \right) \right], \quad (2.7)$$

where $\hat{k}_i = k_i/|\vec{k}|$ denotes the direction of the Fourier wave-vector and δ_s reminds that we are considering here only the effects of the scalar modes of the geometry which are, as already mentioned, the most difficult (but also the most relevant) when the plasma is effectively magnetized.

³Our conventions on the perturbations are summarized by Eq. (2.7). It should be borne in mind that the signature of the metric is mostly minus (see Eq. (2.1)). Various treatments of this problem adopt the opposite convention (i.e. the signature $(-, +, +, +)$).

2.1 CDM particles and neutrinos

Defining as δ_c and θ_c the density contrast of CDM particles and the three-divergence of the corresponding peculiar velocity, the evolution equations of the CDM sector are:

$$\delta'_c = -\theta_c + \frac{h'}{2}, \quad \theta'_c + \mathcal{H}\theta_c = 0. \quad (2.8)$$

In spite of the fact that the CDM velocity field will be used, in Section 3 to remove partially the remaining gauge freedom, it is relevant to appreciate that Eq. (2.8) can be also written as

$$\left(\delta_c - \frac{h}{2}\right)'' + \mathcal{H}\left(\delta_c - \frac{h}{2}\right)' = 0. \quad (2.9)$$

Defining, in analog terms, δ_ν and θ_ν as the neutrino density contrast and as the three-divergence of the neutrino peculiar velocity, the corresponding evolution equations are:

$$\delta'_\nu = -\frac{4}{3}\theta_\nu + \frac{2}{3}h', \quad (2.10)$$

$$\theta'_\nu = -k^2\sigma_\nu + \frac{k^2}{4}\delta_\nu, \quad (2.11)$$

$$\sigma'_\nu = \frac{4}{15}\theta_\nu - \frac{3}{10}k\mathcal{F}_{\nu 3} - \frac{2}{15}h' - \frac{4}{5}\xi', \quad (2.12)$$

where σ_ν is the neutrino anisotropic stress (also appearing in the perturbed Einstein equations) which is related to the quadrupole of the (perturbed) phase space distribution as $\sigma_\nu = \mathcal{F}_{\nu 2}/2$; $\mathcal{F}_{\nu 3}$ is the octupole of the (perturbed) phase space distribution. The presence of the quadrupole and octupole reflects the occurrence that neutrinos are collisionless below temperatures of the order of the MeV and should therefore be treated in the framework of the appropriate Boltzmann hierarchy. Equations (2.10), (2.11) and (2.12) couple together the lowest multipoles and will be the ones used, in Section 3, to set initial conditions of the CMB anisotropies in the pre-equality regime. At later time, in the code, the neutrinos will be integrated using the perturbed form of the collisionless Boltzmann equation written in the synchronous coordinate system:

$$\mathcal{F}'_\nu + ik\mu\mathcal{F}_\nu = 4\left[-\xi' + \frac{\mu^2}{2}(h' + 6\xi')\right], \quad (2.13)$$

where $\mu = \hat{k} \cdot \hat{n}$. Equations (2.10), (2.11) and (2.12) can be derived from Eq. (2.13) by expanding \mathcal{F}_ν in series of Legendre polynomials according to the convention:

$$\mathcal{F}_\nu(\vec{k}, \hat{n}, \tau) = \sum_{\ell} (-i)^\ell (2\ell + 1) \mathcal{F}_{\nu\ell}(k, \tau) P_\ell(\mu). \quad (2.14)$$

For larger multipoles Eqs. (2.10), (2.11) and (2.12) can be written as

$$\mathcal{F}'_{\nu\ell} = \frac{k}{2\ell + 1} [\ell\mathcal{F}_{\nu(\ell-1)} - (\ell + 1)\mathcal{F}_{\nu(\ell+1)}], \quad \ell \geq 3. \quad (2.15)$$

Equation (2.15) can be derived from Eq. (2.13) if we multiply both sides by $P_\ell(\mu)$, i.e. by a generic Legendre Polynomial. By then integrating over μ (between -1 and 1) and by using the convention established in Eq. (2.14), Eq. (2.15) follows by appropriate use of the recurrence relation of the Legendre polynomials stipulating that $(\ell + 1)P_{\ell+1}(\mu) = (2\ell + 1)\mu P_\ell(\mu) - \ell P_{\ell-1}(\mu)$ [48, 49]. The numerical integration will demand to cut the hierarchy at an appropriately (large) multipole. The neutrino fraction in the pre-equality plasma will be denoted by R_ν and it is defined as:

$$R_\nu = \frac{r}{1+r}, \quad r = \frac{7}{8}N_\nu \left(\frac{4}{11}\right)^{4/3} \equiv 0.681 \left(\frac{N_\nu}{3}\right). \quad (2.16)$$

By definition, the photon fraction at the corresponding time will be given by $R_\gamma = 1 - R_\nu$.

2.2 Pre-decoupling plasma

Overall, the plasma will obey the Gauss constraint whose explicit form can be expressed, in the present case, as

$$\vec{\nabla} \cdot \vec{E} = 4\pi e(n_i - n_e), \quad \vec{E} = a^2 \vec{\mathcal{E}}, \quad (2.17)$$

where n_e is the electron concentration and n_i is the concentration of the ions (to be soon identified with protons); \vec{E} is the electric field rescaled through the second power of the scale factor⁴. Electrons and ions are approximately in thermal equilibrium for temperatures smaller than the MeV. The electric field appearing in the Gauss constraint will be screened for length scales $L > \lambda_D$:

$$\lambda_D(\tau_{\text{eq}}) = \sqrt{\frac{T}{8\pi e^2 n_0}} = 2.8 \left(\frac{\omega_M}{0.134}\right)^{-1} \left(\frac{\omega_b}{0.023}\right)^{-1/2} \left(\frac{T}{\text{eV}}\right)^{-1} \text{ m}, \quad (2.18)$$

where $T \simeq T_e \simeq T_i \simeq T_\gamma$. In Eq. (2.18) the common value of the electron and ion concentrations is simply given by

$$n_0 = n_e = n_i = \eta_b n_\gamma, \quad \eta_b = 6.27 \times 10^{-10} \left(\frac{\omega_b}{0.023}\right), \quad (2.19)$$

where the ionization fraction x_e is set to 1 as it is consistent for pre-recombination temperatures. Since the Hubble rate at equality is given by $H_{\text{eq}} = 1.65 \times 10^{-56} (\omega_M/0.134)^2 M_P$ we have that

$$H_{\text{eq}} \lambda_D(\tau_{\text{eq}}) \simeq 2.85 \times 10^{-21} \left(\frac{\omega_M}{0.134}\right) \left(\frac{\omega_b}{0.023}\right)^{-1/2} \left(\frac{T}{\text{eV}}\right)^{-1}. \quad (2.20)$$

The hierarchy between the Debye length λ_D and the other length-scales of the problem persists if we move from the equality time to the decoupling time. According to Eq. (2.18) λ_D scales⁵ as $a(\tau)$ (since $T \simeq a^{-1}$ and $n_0 \simeq a^{-3}$). Thus $\lambda(\tau_{\text{dec}}) \simeq 3(\omega_M/0.134)\lambda_{\text{eq}}$ where the factor $3(\omega_M/0.134)$ arises because $(a_{\text{dec}}/a_{\text{eq}}) \simeq 2.393(\omega_M/0.134)$ (taking, as an example, $1 + z_{\text{dec}} \simeq 1100$ and fixing the ionization fraction as $x_e \simeq 1$).

Recombination entails a sudden drop in the ionization fraction. From the usual considerations involving Saha's equation, around decoupling, $x_e \simeq 10^{-5}$. The Debye length increases then (see Eq. (2.18)) by a factor $10^{2.5}$ which is still minute in comparison with all the other lengths of the problem. Note that $\lambda_D(\tau_{\text{dec}})$ is not only parametrically smaller than the Hubble radius, but it is also negligible in comparison with the sound horizon at the corresponding epoch, i.e.

$$r_s(\tau_{\text{dec}}) = \int_0^{\tau_{\text{dec}}} d\tau c_{\text{sb}}(\tau) = \int_0^{\tau_{\text{dec}}} \frac{d\tau}{\sqrt{3[1 + R_b(\tau)]}}, \quad (2.21)$$

where $c_{\text{sb}}(\tau)$ (the characteristic sound speed of the baryon-photon system in the tight coupling approximation) is defined in terms of the baryon to photon ratio R_b (see also Eqs. (2.83) and (3.1)):

$$R_b(z) = \frac{3}{4} \frac{\rho_b}{\rho_\gamma} = 0.664 \left(\frac{\omega_b}{0.023}\right) \left(\frac{1051}{z+1}\right). \quad (2.22)$$

⁴In the present paper we will denote with calligraphic style the electric and magnetic fields which are not rescaled through a^2 , i.e. $\vec{E} = a^2 \vec{\mathcal{E}}$ and $\vec{B} = a^2 \vec{\mathcal{B}}$.

⁵In principle the electron and baryon temperature (in the absence of energy exchange and in the absence of photons) should scale as a^{-2} . However, as it will be discussed in a moment, the Coulomb and Thompson rates of interactions are both larger than the Hubble rate and $T_e \simeq T_i \simeq T_\gamma = T$ (see Eqs. (2.30)–(2.35) and discussions therein).

Since the dark energy component is negligible around decoupling the integral appearing in Eq. (2.21) can be estimated analytically and the overall result can be expressed as:

$$\frac{r_s(\tau_{\text{dec}})}{\text{Mpc}} = \frac{2998}{\sqrt{1+z_{\text{dec}}}} \frac{2}{\sqrt{3}\omega_M c_1} \ln \left[\frac{\sqrt{1+c_1} + \sqrt{c_1+c_1 c_2}}{1 + \sqrt{c_1 c_2}} \right], \quad (2.23)$$

where

$$c_1 = 27.6 \omega_b \left(\frac{1100}{1+z_{\text{dec}}} \right), \quad c_2 = \frac{0.045}{h_0^2 \omega_M} \left(\frac{1+z_{\text{dec}}}{1100} \right). \quad (2.24)$$

With our fiducial values of the parameters, $r_s(\tau_{\text{dec}})$ lies between 150 and 200 Mpc. But now this figure should be compared with the Debye length $\lambda(\tau_{\text{dec}}) \simeq 2.5 \times 10^3$ m (having taken into account the drop in the ionization fraction). Thus, as anticipated, $\lambda_D(\tau_{\text{dec}})/r_s(\tau_{\text{dec}}) \simeq 10^{-21}$. So the plasma is, to a very good approximation globally neutral.

As already mentioned, for temperatures smaller than the temperature of neutrino decoupling baryons and electrons interact strongly through Coulomb scattering. The corresponding rate, for $T > \text{eV}$, is ⁶:

$$\frac{\Gamma_{\text{Coul}}}{H} \simeq 4 \times 10^{11} x_e \left(\frac{T}{\text{eV}} \right)^{-1/2} \left(\frac{\omega_b}{0.023} \right). \quad (2.25)$$

Since after equality $H \propto T^{3/2}$ (and ignoring for the moment the drop in the ionization fraction) the ratio of Eq. (2.25) gets frozen. Equation (2.25) justifies to consider a unique baryon-lepton fluid as a single dynamical entity. In Eq. (2.25) the Coulomb rate has been computed by recalling that

$$\begin{aligned} \Gamma_{\text{Coul}} &= n_e x_e v_{\text{th}} \sigma_{\text{Coul}}, & v_{\text{th}} &\simeq \sqrt{\frac{T}{m_e}}, \\ \sigma_{\text{Coul}} &= \frac{\alpha_{\text{em}}^2}{T^2} \ln \Lambda_C, & \Lambda_C &= \frac{3}{2} \left(\frac{T^3}{\pi n_e} \right)^{1/2} \frac{1}{e^3}. \end{aligned} \quad (2.26)$$

where $\ln \Lambda_C \simeq 14.71$ for typical values of ω_b . The Coulomb cross section is the main responsible for the conductivity of the plasma which can be estimated as the ratio between the square of the plasma frequency and the Coulomb rate (which is also, by definition, the collision frequency), namely

$$\sigma_c(T) = \frac{\omega_{\text{pe}}^2}{4\pi\Gamma_{\text{Coul}}} = \frac{4\pi}{\alpha_{\text{em}} \ln \Lambda_C} T \left(\frac{T}{m_e} \right)^{1/2} \simeq 0.16 \left(\frac{T}{\text{eV}} \right)^{3/2} \text{ eV}, \quad (2.27)$$

where, as it should, the electron concentration effectively simplifies in the final expression. It is useful also to estimate, at this point, the plasma frequency of the electrons, i.e.

$$\omega_{\text{pe}} = \sqrt{\frac{4\pi e^2 n_e}{m_e}} = 28.05 \sqrt{x_e} \left(\frac{T}{\text{eV}} \right)^{3/2} \left(\frac{\omega_b}{0.023} \right)^{1/2} \text{ MHz}. \quad (2.28)$$

Thus the typical length-scales are much larger than the Debye scale. The typical time-scales greatly exceed ω_{pe}^{-1} . This is the realm of MHD.

Prior to equality electrons and protons interact also with photons via Thompson cross-section. Protons can be neglected in the Thompson mean free path (determined by electron-photon interactions); the Thompson rate in units of the Hubble rate is, for $T > \text{eV}$,

$$\frac{\Gamma_{\text{Th}}}{H} \simeq 5.9 \times 10^4 x_e \left(\frac{\omega_b}{0.023} \right) \left(\frac{T}{\text{eV}} \right). \quad (2.29)$$

⁶In the case of a proton (or of an electron) impinging on an electron (or on a proton) the Rutherford cross section is logarithmically divergent at large impact parameters when the particles are free. In the plasma around decoupling the logarithmic divergence is avoided because of the Debye screening length: the cross section is then known as Coulomb cross section and the logarithmic divergence is replaced by the so-called Coulomb logarithm.

After equality Γ_{Th}/H is proportional to $T^{3/2}$ and it becomes eventually much smaller than one as x_e drops at recombination. Deep in the radiation epoch, i.e. when the initial conditions of CMB anisotropies are set numerically, the Coulomb rate of Eq. (2.25) is larger than the Thompson rate but while the Thompson rate increases with the temperature (see Eq. (2.29)) the Coulomb rate decreases. The meeting point of the two rates occurs close to the MeV. Initial conditions will then be set in the radiation epoch when both Coulomb and Thompson scattering are large. Also photons are strongly coupled to the baryon-lepton fluid. So, a unique physical entity emerges, i.e. the so-called baryon-lepton-photon fluid. This fluid is often dubbed as the baryon-photon fluid by implicitly including the electrons in the baryonic component thanks to the strength of Coulomb coupling.

The various species have all a putative common temperature T , i.e. $T_e \simeq T_p \simeq T_\gamma = T$. This statement will now be justified. Electrons and protons, being massive, have energy densities and pressures which can be written, respectively, as

$$\rho_e = n_e \left[m_e + \frac{3}{2} T_e \right], \quad p_e = n_e T_e, \quad (2.30)$$

$$\rho_p = n_p \left[m_p + \frac{3}{2} T_p \right], \quad p_p = n_p T_p. \quad (2.31)$$

The photon energy density and pressure will be instead, as it is well known, $\rho_\gamma = (\pi^2/15)T_\gamma^4$ and $p_\gamma = \rho_\gamma/3$. Ignoring, for the moment, the other species of the plasma, the total conservation equation assumes the form $d(a^3\rho) + pd(a^3) = 0$ where $\rho = (\rho_e + \rho_p + \rho_\gamma)$ and $p = (p_e + p_p + p_\gamma)$. Since $n_e = n_p = n_0$ (and both scale as a^{-3}) the total conservation equation implies the following differential relation:

$$a\lambda d(aT_\gamma) + d[a^2(T_e + T_p)] = 0, \quad \lambda = 2.8 \times 10^9 \left(\frac{\omega_b}{0.023} \right)^{-1}. \quad (2.32)$$

Up to numerical factors λ is the ratio between the entropy density of the photons and n_0 which is, in turn, roughly 10 orders of magnitude smaller than the photon concentration. The electron and proton temperatures vary adiabatically as a^{-2} (in the absence of photons) while the radiation temperature varies as a^{-1} (in the absence of protons and electrons). But we do know that electron-photon and electron-proton interactions tie the temperatures close together. Equation (2.32) can then be solved assuming, to lowest order, $T_e \simeq T_p \simeq T_\gamma = T$. The differences in the various temperatures can be estimated: if the differences are small the assumption of a common temperature is justified. To lowest order Eq. (2.32) becomes

$$\frac{d \ln T_\gamma}{d \ln a} = -\frac{\lambda + 4}{\lambda + 2}, \quad T_\gamma \simeq a^{-1 - \frac{2}{\lambda}}, \quad (2.33)$$

where the second relation is obtained from the first one after expanding the obtained result in powers of $1/\lambda$. Equation (2.33) shows that, indeed, T_γ evolves in a way which is intermediate between a^{-1} (as implied in the absence of electrons and protons) and a^{-2} . The differences between the T_γ , T_e and T_p depend upon the Thompson and Coulomb rates. The rate of gain of energy per electron as well as the rates of gain of electron and proton thermal energies can be written as

$$\begin{aligned} \frac{1}{a^2} \frac{d(a^2 T_e)}{dt} &= -\Gamma_{\text{Th}}(T_e - T_\gamma) - \Gamma_{\text{Coul}}(T_e - T_p), \\ \frac{1}{a^2} \frac{d(a^2 T_p)}{dt} &= -\Gamma_{\text{Coul}}(T_p - T_e), \quad \frac{\lambda}{a} \frac{d(a T_\gamma)}{dt} = -\Gamma_{\text{Th}}(T_\gamma - T_e), \end{aligned} \quad (2.34)$$

Equation (2.34) implies, as expected, that

$$\frac{T_\gamma - T_e}{T} \simeq 2 \frac{H}{\Gamma_{\text{Th}}}, \quad \frac{T_e - T_p}{T} \simeq \frac{H}{\Gamma_{\text{Coul}}}. \quad (2.35)$$

The same hierarchy between Coulomb and Thompson scattering rates also determines the small temperature differences between electrons, protons and photons. Thus electron-proton collisions are sufficiently fast to assess that electrons and protons have indeed the same putative temperature.

2.3 The baryon-lepton-photon fluid

The strength of the Coulomb coupling implies that, effectively, there is a unique velocity field which is the centre of mass velocity of the electron-proton fluid, i.e.

$$\vec{v}_b = \frac{m_e \vec{v}_e + m_p \vec{v}_p}{m_e + m_p}. \quad (2.36)$$

The velocity \vec{v}_b is the bulk velocity of the plasma [5, 6]. The evolution equation of \vec{v}_b can be obtained by summing up the evolution equations of electrons and ions [6], as it happens in the usual MHD treatment of the problem. In the synchronous gauge, the baryon velocity and the baryon density contrast obey, respectively, the following pair of equations

$$\delta'_b = -\theta_b + \frac{h'}{2} + \frac{\vec{E} \cdot \vec{J}}{a^4 \rho_b}, \quad (2.37)$$

$$\theta'_b + \mathcal{H}\theta_b = \frac{4}{3} \frac{\rho_\gamma}{\rho_b} \epsilon' (\theta_\gamma - \theta_b) + \frac{\vec{\nabla} \cdot [\vec{J} \times \vec{B}]}{a^4 \rho_b}. \quad (2.38)$$

where, the divergence of the baryon velocity and the differential optical depth have been introduced as

$$\theta_b = \vec{\nabla} \cdot \vec{v}_b, \quad \epsilon' = x_e \frac{a}{a_0} \sigma_T n_e. \quad (2.39)$$

Equation (2.38) has been written, unlike the analog equations for CDM and neutrinos, not in Fourier space but in real space to emphasize the presence of a new term which is nothing but the MHD form of the Lorentz force given by $\vec{J} \times \vec{B}$ where \vec{J} is the Ohmic current and \vec{B} is the magnetic field. The electric field appearing in Eq. (2.37) is negligible since, in the plasma frame, the conductivity effectively suppresses the Ohmic electric fields.

According to Eq. (2.38) the baryon-lepton fluid exchanges momentum with the photons. The lowest two multipoles of the Boltzmann hierarchy of the photons, namely the density contrast (i.e. the monopole) and the three-divergence of the velocity field (related to the dipole of the intensity of the brightness perturbations) are:

$$\delta'_\gamma = -\frac{4}{3}\theta_\gamma + \frac{2}{3}h', \quad (2.40)$$

$$\theta'_\gamma = -\frac{1}{4}\nabla^2 \delta_\gamma + \epsilon'(\theta_b - \theta_\gamma). \quad (2.41)$$

While the sum of the electron and proton equations leads to Eq. (2.38), their difference leads to the Ohm law [5, 6] which relates the total current \vec{J} to the electric field through the conductivity, i.e.

$$\vec{J} = \sigma(\vec{E} + \vec{v}_b \times \vec{B}), \quad \sigma = \sigma_c a, \quad \vec{J} = a^3 \vec{j}, \quad (2.42)$$

where σ_c denotes the flat-space conductivity; furthermore, as already mentioned, $\vec{B} = a^2 \vec{\mathcal{B}}$ and $\vec{E} = a^2 \vec{\mathcal{E}}$. The usefulness of the latter rescalings can be understood by looking also at the other MHD

equations, namely

$$\vec{\nabla} \cdot \vec{E} = 0, \quad \vec{\nabla} \cdot \vec{B} = 0, \quad (2.43)$$

$$\vec{\nabla} \times \vec{B} = 4\pi \vec{J}, \quad \frac{\partial \vec{B}}{\partial \tau} + \vec{\nabla} \times \vec{E} = 0. \quad (2.44)$$

Equations (2.43) and (2.44) have the same form they would have in flat space. The space-time is however curved and with line element given by Eq. (2.1). Maxwell equations in conformally flat backgrounds are known to be invariant under a Weyl rescaling of the metric. Consequently the corresponding evolution equations have exactly the same form they would have in Minkowskian space-time provided the field are appropriately rescaled and provided the conformal time coordinate τ is consistently employed.

The displacement current does not appear in Eq. (2.44). Indeed MHD is a description that holds for typical length-scales that are larger than the Debye length and for typical time-scales that are much larger than the inverse of the plasma frequency. In other words, if we are interested to study the high frequency branch of the spectrum of plasma excitations we should resort to a full kinetic (Vlasov-Landau) description [6]. The Ohmic current can then be related to the magnetic field, i.e.

$$\vec{J} = \frac{1}{4\pi} \vec{\nabla} \times \vec{B}, \quad \vec{\nabla} \cdot \vec{J} = 0. \quad (2.45)$$

Thus, the total current, the electric field and the magnetic field are all solenoidal albeit for rather different physical reasons. Equation (2.45) can be used to compute explicitly the Ohmic electric field, i.e.

$$\vec{E} = -\vec{v}_b \times \vec{B} + \frac{\vec{\nabla} \times \vec{B}}{4\pi\sigma}, \quad (2.46)$$

which shows that electric fields vanish, at finite conductivity, in the baryon rest frame. They are therefore smaller than the magnetic fields since, as previously shown explicitly, the pre-decoupling plasma is an excellent conductor. The latter statement defines the plasma frame, i.e. the frame where, thanks to the large value of the conductivity, the electric fields vanish while the magnetic field are not dissipated, by conductivity, at large scales.

Also magnetic fields are affected by conductivity but to a lesser extent and only at sufficiently short scales (which are already erased by the finite value of the thermal diffusivity scale, i.e. Silk damping). The typical magnetic diffusivity scale (i.e. the length-scale below which the magnetic field is dissipated by the finite value of the conductivity) can be understood from the corresponding magnetic diffusivity equation. Inserting Eq. (2.46) into the second relation of Eq. (2.44) the magnetic diffusivity equation can be written as:

$$\frac{\partial \vec{B}}{\partial \tau} = \vec{\nabla} \times (\vec{v}_b \times \vec{B}) + \frac{\nabla^2 \vec{B}}{4\pi\sigma}. \quad (2.47)$$

According to Eq. (2.47) the magnetic field power spectrum will be diffused for typical wave-numbers $k > k_\sigma \simeq \sqrt{4\pi\sigma_c H}$. Thus, only sufficiently short length-scales $L < L_\sigma \simeq k_\sigma^{-1}$ are dissipated. The ratio of L_σ to the Hubble radius, i.e. $L_\sigma H$, being suppressed by (T/M_p) , is always minute. Around equality we can estimate that $L_\sigma H \simeq 3.9 \times 10^{-17} (T/\text{eV})^{1/4}$ where σ_c is given by Eq. (2.27).

For $T < \text{MeV}$ the kinetic Reynolds number is smaller than one. This property is not verified, for instance, during the life of spiral galaxies where, effectively, the kinetic energy of the plasma can be converted into magnetic energy by means of the first term of Eq. (2.47) which is often dubbed dynamo term [9]. When the kinetic Reynolds number is small (i.e. in the absence of kinetic turbulence)

the plasma description following from MHD can be also phrased in terms of the conservation of two interesting quantities, i.e. the magnetic flux and the magnetic helicity [7]:

$$\frac{d}{dt} \left(\int_{\Sigma} \vec{B} \cdot d\vec{\Sigma} \right) = -\frac{1}{4\pi\sigma} \int \vec{\nabla} \times \vec{\nabla} \times \vec{B} \cdot d\vec{\Sigma}, \quad (2.48)$$

$$\frac{d}{dt} \left(\int_V d^3x \vec{A} \cdot \vec{B} \right) = -\frac{1}{4\pi\sigma} \int_V d^3x \vec{B} \cdot \vec{\nabla} \times \vec{B}. \quad (2.49)$$

In Eq. (2.48), Σ is an arbitrary finite surface that moves with the plasma. In the ideal MHD limit (i.e. $\sigma = a\sigma_c \rightarrow \infty$) the magnetic flux is conserved. In the same limit also the magnetic helicity is conserved. In the resistive limit the magnetic flux and helicity are dissipated with a rate proportional to $1/\sigma$ which is small provided the conductivity is sufficiently high. The term appearing at the right hand side of Eq. (2.49) is called magnetic gyrotropy. Since, at high temperatures, the conductivity grows with T the ideal limit is always verified better and better as we go back in time.

The conservation of the magnetic helicity is a statement on the conservation of the topological properties of the magnetic flux lines. If the magnetic field is completely stochastic, the magnetic flux lines will be closed loops evolving independently in the plasma and the helicity will vanish. There could be, however, more complicated topological situations where a single magnetic loop is twisted (like some kind of Möbius stripe) or the case where the magnetic loops are connected like the rings of a chain. In both cases the magnetic helicity will not be zero since it measures, essentially, the number of links and twists in the magnetic flux lines. The magnetic helicity will have no impact on our considerations since the scalar fluctuations of the geometry are not affected by the helical features of the magnetic fields. On the contrary in the vector and tensor cases the situation can be different [44].

In the resistive MHD approximation the electric components of the energy-momentum tensor can be neglected, while the magnetic components are present only at sufficiently large scales $L > L_\sigma$:

$$\mathcal{T}_0^0(\vec{x}, \tau) = \frac{B^2}{8\pi a^4}, \quad \mathcal{T}_i^j(\vec{x}, \tau) = \frac{1}{4\pi a^4} \left[B_i B^j - \frac{B^2}{2} \delta_i^j \right] \quad (2.50)$$

where $B^2 = B_i B^i$. In Eq. (2.50) the contribution of the electric terms can be neglected since they are all suppressed by two powers of the conductivity. The Poynting vector can be also neglected since, at finite conductivity is suppressed as σ^{-1}

$$\mathcal{T}_0^i(\vec{x}, \tau) = \frac{1}{4\pi a^4} \vec{E} \times \vec{B} \simeq \frac{1}{4\pi a^4 \sigma} \vec{J} \times \vec{B}, \quad (2.51)$$

where Eq. (2.44) has been used in the second equality. The spatial components of the energy momentum tensor can be phrased in terms of the magnetic pressure and of the anisotropic stress, i.e.

$$\mathcal{T}_i^j(\vec{x}, \tau) = -\delta p_B(\vec{x}, \tau) \delta_i^j + \tilde{\Pi}_i^j(\vec{x}, \tau), \quad \mathcal{T}_0^0(\vec{x}, \tau) = \delta p_B(\vec{x}, \tau), \quad (2.52)$$

where, with standard notations:

$$\delta p_B(\vec{x}, \tau) = \frac{B^2(\vec{x})}{8\pi a^4}, \quad \delta p_B = \frac{\delta \rho_B}{3}, \quad (2.53)$$

$$\tilde{\Pi}_i^j(\vec{x}, \tau) = \frac{1}{4\pi a^4} \left[B_i B^j - \frac{B^2}{3} \delta_i^j \right]. \quad (2.54)$$

It is practical to refer the magnetic fields to the photon background by means of the following rescaling

$$\Omega_B(\vec{x}, \tau) = \frac{\delta p_B(\vec{x}, \tau)}{\rho_\gamma(\tau)} \equiv \frac{B^2(\vec{x}, \tau)}{8\pi \bar{\rho}_\gamma}, \quad \partial_j \partial^i \tilde{\Pi}_i^j = (p_\gamma + \rho_\gamma) \nabla^2 \sigma_B. \quad (2.55)$$

where $\bar{\rho}_\gamma = a^4 \rho_\gamma$. With the notations of Eq. (2.55) the identity

$$\nabla^2 \sigma_B = \frac{3}{16\pi\bar{\rho}_\gamma} \partial_i B_j \partial^j B^i - \frac{1}{2} \nabla^2 \Omega_B \quad (2.56)$$

allows to express the three-divergence of the Lorentz force appearing in Eq. (2.38) in terms of Ω_B and σ_B :

$$\frac{3}{4} \frac{\vec{\nabla} \cdot [\vec{J} \times \vec{B}]}{\bar{\rho}_\gamma} = \nabla^2 \sigma_B - \frac{1}{4} \nabla^2 \Omega_B. \quad (2.57)$$

Stochastically distributed large-scale magnetic fields do not break the spatial isotropy of the background geometry introduced in Eq. (2.1). Nearly all magnetogenesis mechanisms suggest indeed that the large-scale magnetic fields should be stochastically distributed and characterized by their two-point function. Defining the Fourier amplitude of the magnetic fields as

$$B_i(\vec{x}) = \frac{1}{(2\pi)^{3/2}} \int d^3k B_i(k) e^{-i\vec{k}\cdot\vec{x}}, \quad (2.58)$$

their two-point function can be expressed as

$$\langle B_i(\vec{k}) B_j(\vec{p}) \rangle = \frac{2\pi^2}{k^3} P_{ij}(k) P_B(k) \delta^{(3)}(\vec{k} + \vec{p}), \quad (2.59)$$

where

$$P_{ij}(k) = \left(\delta_{ij} - \frac{k_i k_j}{k^2} \right), \quad P_B(k) = \mathcal{A}_B \left(\frac{k}{k_L} \right)^{n_B - 1}. \quad (2.60)$$

In Eq. (2.60) n_B is the magnetic spectral index and \mathcal{A}_B is the amplitude ⁷ of the magnetic power spectrum referred to the magnetic pivot scale k_L . In terms of this definition the two-point function of the magnetic fields in real space can be written as

$$\langle B_i(\vec{x}) B_j(\vec{y}) \rangle = \int d \ln k P_{ij}(k) P_B(k) \frac{\sin kr}{kr}, \quad r = |\vec{x} - \vec{y}| \quad (2.61)$$

Different conventions exist in the literature for assigning the magnetic power spectrum. For instance in [28, 29] the k^{-3} (appearing at the right hand side of Eq. (2.59)) was included in the definition of $P_B(k)$. Those authors, indeed, only dealt with tensor and vector modes and were not confronted with the necessity of assigning power spectra according to the standards of CMB physics. We are forced on Eqs. (2.58)–(2.60) since these are the conventions used to define the power spectrum of curvature perturbations (see for instance [11, 12, 13, 14]) and it would be strange to use normalizations and definitions of the spectral indices that may differ from the ones which are commonly established when presenting theoretical and observational studies of the parameter space of CMB anisotropies.

2.4 Gravitating magnetic fields

All the species introduced so far gravitate and, therefore, affect the evolution of the metric perturbations ξ and h . In Fourier space, the Hamiltonian and the momentum constraints stemming from the

⁷Note that, according to Eq. (2.58), the dimensions of $B_i(\vec{x})$ are of L^{-2} . Thus, dimensionally, $[B_i(k)] = L$. But then it is easy to see (taking into account the dimensions of the three-dimensional Dirac delta function) that, dimensionally, $[\mathcal{A}_B] = L^{-4}$, i.e. \mathcal{A}_B (and hence $P_B(k)$) has the same dimensions of the magnetic energy density in real space. This is another good reason, unlike previous studies (see [29] last three references), to follow the conventions expressed by Eq. (2.59).

(00) and (0*i*) components of the perturbed Einstein equations are, respectively

$$2k^2\xi - \mathcal{H}h' = 8\pi G a^2[\delta\rho_t + \delta\rho_B], \quad (2.62)$$

$$k^2\xi' = -4\pi G a^2(p_t + \rho_t)\theta_t. \quad (2.63)$$

In Eqs. (2.62) and (2.63) $\delta\rho_t$ and θ_t are the global density fluctuation of the plasma and the total velocity field defined as

$$\delta\rho_t = \delta\rho_c + \delta\rho_\nu + \delta\rho_\gamma + \delta\rho_b, \quad (2.64)$$

$$(p_t + \rho_t)\theta_t = \sum_a (p_a + \rho_a)\theta_a \equiv \frac{4}{3}\rho_\nu\theta_\nu + \frac{4}{3}\rho_\gamma\theta_\gamma + \rho_c\theta_c + \rho_b\theta_b. \quad (2.65)$$

The spatial components of the perturbed Einstein equations (i.e., respectively, ($i = j$) and ($i \neq j$)) lead instead to:

$$h'' + 2\mathcal{H}h' - 2k^2\xi = 24\pi G a^2[\delta p_t + \delta p_B], \quad (2.66)$$

$$(h + 6\xi)'' + 2\mathcal{H}(h + 6\xi)' - 2k^2\xi = 24\pi G a^2[(p_\nu + \rho_\nu)\sigma_\nu + (p_\gamma + \rho_\gamma)\sigma_B]. \quad (2.67)$$

In Eq. (2.67) the neutrino anisotropic stress (also appearing in Eqs. (2.11) and (2.12)) has been consistently included. For analytical estimates it is also useful to write the evolution equation for the total density contrast which reads, in the synchronous gauge,

$$\delta\rho_t' + 3\mathcal{H}(c_{st}^2 + 1)\delta\rho_t + 3\mathcal{H}\delta p_{nad} + (p_t + \rho_t)\theta_t - (p_t + \rho_t)\frac{h'}{2} = 0, \quad (2.68)$$

where the total sound speed c_{st}^2 and the non-adiabatic pressure fluctuation δp_{nad} have been introduced. Their respective definitions can be extracted from the following pair of relations:

$$\delta p_t = c_{st}^2\delta\rho_t + \delta p_{nad}, \quad c_{st}^2 = \frac{p_t'}{\rho_t'}. \quad (2.69)$$

Equation (2.69) implies that the pressure fluctuations can be generated either by inhomogeneities in the energy density or by fluctuations of the sound speed itself. The latter fluctuations are non-adiabatic in nature since they arise, physically, as a fluctuation of the specific entropy, i.e. the entropy density of the photon gas measured in units of the concentration of another given species. This property is customarily used to classify the initial conditions of CMB anisotropies which are therefore divided into adiabatic and non-adiabatic.

In the case of the adiabatic mode, by definition, the fluctuations in the entropy density vanish over typical scales larger than the Hubble radius at recombination. The opposite holds for the non-adiabatic modes. In the case of the CDM-radiation mode the specific entropy is just given by $\varsigma = T^3/n_c$ where n_c is the concentration of the CDM particles. The entropy fluctuations (i.e. the relative fluctuations in the specific entropy) are given by

$$\mathcal{S} = \frac{\delta\varsigma}{\varsigma} = \frac{3}{4}\delta_\gamma - \delta_c. \quad (2.70)$$

More generally, given two species of the plasma the entropy fluctuations are defined as [45, 46, 47]

$$\mathcal{S}_{ij} = -\left(\frac{\delta_i}{w_i + 1} - \frac{\delta_j}{w_j + 1}\right). \quad (2.71)$$

The non-adiabatic pressure fluctuations can then be written as⁸:

$$\delta p_{\text{nad}} = \frac{1}{6\mathcal{H}\rho'_t} \sum_{ij} \rho'_i \rho'_j (c_{s_i}^2 - c_{s_j}^2) \mathcal{S}_{ij}, \quad c_{s_i}^2 = \frac{p'_i}{\rho'_i}, \quad (2.72)$$

where $c_{s_i}^2$ and $c_{s_j}^2$ are sound speeds of two (generic) species. Thus, according to Eq. (2.72), δp_{nad} measures, indeed, the degree of compositeness of the plasma: if more species are present, more non-adiabatic modes are possible and δp_{nad} receives more contributions. In the pre-equality plasma there are four (regular) non-adiabatic modes (i.e. the CDM-radiation mode, the baryon-radiation mode, the neutrino density and the neutrino isocurvature modes). There is one adiabatic mode whose presence is strongly suggested by the analysis of cosmological data in the framework of a Λ CDM scenario. This does not exclude the presence of a dominant adiabatic mode with a subdominant non-adiabatic component (see, for instance, [51]).

The analysis will be here limited to the case of a single adiabatic mode in the presence of large-scale magnetic fields. This is the minimal situation compatible with the Λ CDM framework. Our code can accommodate also non-adiabatic initial conditions in the presence of magnetic fields. The initial conditions discussed in [32], if appropriately translated to the synchronous frame, allow for this possibility. Mixed initial conditions involve a dominant magnetized adiabatic mode and a number of magnetized non-adiabatic modes with subdominant amplitude.

Two variables are customarily used to parametrize the power spectrum of the metric fluctuations. They will be denoted by \mathcal{R} and by ζ . In terms of the synchronous degrees of freedom, they can be defined as

$$\mathcal{R} = \xi + \frac{\mathcal{H}\xi'}{\mathcal{H}^2 - \mathcal{H}'}, \quad \zeta = \xi - \frac{\mathcal{H}(\delta\rho_t + \delta\rho_B)}{\rho'_t}. \quad (2.73)$$

Even if both \mathcal{R} and ζ are gauge-invariant, their physical interpretation is obtained by expressing the two variables in specific gauges: \mathcal{R} is often dubbed curvature perturbation since it corresponds, in the comoving orthogonal gauge, to the perturbations of the spatial curvature. In analog terms, ζ is interpreted as the curvature perturbation in the gauge where the density contrast vanishes (also called uniform density gauge). Taking the difference of \mathcal{R} and ζ and using the Hamiltonian constraint (2.62), the following equation can be obtained:

$$\zeta - \mathcal{R} = -\frac{2k^2\xi - (h + 6\xi)'}{24\pi G a^2(p_t + \rho_t)} \quad (2.74)$$

The quantity at the right hand side of Eq. (2.74) is $\mathcal{O}(k^2\tau^2)$ and, therefore, it is negligible when the relevant wavelengths are larger than the Hubble radius, in particular around equality. This property can be immediately understood by expressing the combination at the right hand side of Eq. (2.74) in terms of longitudinal gauge variables and, most notably, ψ which denotes the spatial fluctuation of the metric in the longitudinal gauge:

$$\zeta - \mathcal{R} = -\frac{k^2\psi}{12\pi G a^2(p_t + \rho_t)}, \quad \psi = -\xi + \frac{h' + 6\xi'}{2k^2}. \quad (2.75)$$

In the longitudinal gauge ψ is constant, to lowest order, when the relevant wavelengths are larger than the Hubble radius (see Appendix A). The evolution of ζ on scales larger than the Hubble radius translates immediately in the evolution of \mathcal{R} . The evolution of ζ can be simply obtained by inserting

⁸Owing to their definitions, both \mathcal{S}_{ij} and δp_{nad} are gauge-invariant.

Eq. (2.73) into Eq. (2.68). The logic is to trade $\delta\rho_t$ in favor of ζ . The result of this manipulation, after the use of the covariant conservation equation of the total fluid (i.e. Eq. (2.4)), is:

$$\zeta' = -\frac{\mathcal{H}}{p_t + \rho_t}\delta p_{\text{nad}} + \frac{\mathcal{H}}{p_t + \rho_t}\left(c_{\text{st}}^2 - \frac{1}{3}\right)\delta\rho_{\text{B}} - \frac{\bar{\theta}_t}{3}, \quad \bar{\theta}_t = \theta_t - \frac{h' + 6\xi'}{2}, \quad (2.76)$$

where $\bar{\theta}_t$ is the three-divergence of the velocity field in the longitudinal gauge (see the Appendix, Eq. (A.2)). If $\delta p_{\text{nad}} = 0$ (as contemplated in the present paper), then Eq. (2.76) can be explicitly integrated with the result that

$$\zeta(k, \tau) = \zeta_*(k) - \frac{3R_\gamma\Omega_{\text{B}}(k)\alpha}{4(3\alpha + 4)}, \quad (2.77)$$

where $\alpha = a/a_{\text{eq}}$ and $R_\gamma = 1 - R_\nu$ (see Eq. (2.16)). So the spectrum of the primordial adiabatic mode will be given in terms of $\zeta_*(k) = \mathcal{R}_*(k)$. The two-point function in Fourier space will be, for \mathcal{R}

$$\langle \mathcal{R}_*(\vec{k}, \tau)\mathcal{R}_*(\vec{p}, \tau) \rangle = \frac{2\pi^2}{k^3}\mathcal{P}_{\mathcal{R}}(k)\delta^{(3)}(\vec{k} + \vec{p}), \quad \mathcal{P}_{\mathcal{R}}(k) = \mathcal{A}_{\mathcal{R}}\left(\frac{k}{k_{\text{p}}}\right)^{n_{\text{s}}-1}, \quad (2.78)$$

where n_{s} is the scalar (adiabatic) spectral index, $k_{\text{p}} = 0.002 \text{ Mpc}^{-1}$ is the so-called pivot scale and $\mathcal{A}_{\mathcal{R}}$ is, by definition, the amplitude of the power spectrum at the pivot scale. With these conventions the two-point function in real space becomes

$$\langle \mathcal{R}_*(\vec{x}, \tau)\mathcal{R}_*(\vec{y}, \tau) \rangle = \int d\ln k \mathcal{P}_{\mathcal{R}}(k) \frac{\sin kr}{kr}, \quad r = |\vec{x} - \vec{y}| \quad (2.79)$$

So far the evolution equations of the lowest multipoles of the Boltzmann hierarchy have been introduced. It is relevant to recall also the brightness perturbations of the radiation field which are related to the inhomogeneities of the Stokes parameters. In the synchronous coordinate system the evolution equations of the brightness perturbations can be written as

$$\Delta'_{\text{I}} + ik\mu\Delta_{\text{I}} = -\left[\xi' - \frac{\mu^2}{2}(h' + 6\xi')\right] + \epsilon'\left[-\Delta_{\text{I}} + \Delta_{\text{I}0} + \mu v_{\text{b}} - \frac{1}{2}P_2(\mu)S_{\text{Q}}\right], \quad (2.80)$$

$$\Delta'_{\text{Q}} + ik\mu\Delta_{\text{Q}} = \epsilon'\left[-\Delta_{\text{Q}} + \frac{1}{2}(1 - P_2(\mu))S_{\text{Q}}\right], \quad (2.81)$$

$$\Delta'_{\text{U}} + ik\mu\Delta_{\text{U}} = -\epsilon'\Delta_{\text{U}}, \quad (2.82)$$

$$v'_{\text{b}} + \mathcal{H}v_{\text{b}} + \frac{\epsilon'}{R_{\text{b}}}(3i\Delta_{\text{I}1} + v_{\text{b}}) + ik\frac{\Omega_{\text{B}} - 4\sigma_{\text{B}}}{4R_{\text{b}}} = 0, \quad (2.83)$$

where R_{b} has been defined in Eq. (2.22) and where we defined $v_{\text{b}} = \theta_{\text{b}}/(ik)$. Moreover, in Eqs. (2.80) and (2.81):

$$S_{\text{Q}} = \Delta_{\text{I}2} + \Delta_{\text{Q}0} + \Delta_{\text{Q}2}. \quad (2.84)$$

The notations Δ_{ℓ} and $\Delta_{\text{Q}\ell}$ denote the ℓ -th multipole of Δ_{I} and Δ_{Q} . In Eqs. (2.80) and (2.81) $P_2(\mu) = (3\mu^2 - 1)/2$ is the second Legendre polynomial. Equations (2.80)–(2.83) constitute the basis of the semi-analytical approach used to estimate the magnetized temperature autocorrelations [31, 32, 33]. In particular, the aforementioned equations have been solved in the tight-coupling approximation to first and second order [31, 32]. The physical information contained in Eqs. (2.80)–(2.83) can be summarized by noticing that to zeroth-order in the tight-coupling expansion the CMB is not polarized in the baryon rest frame so that Δ_{Q} and Δ_{U} will be zero. To first-order in the tight-coupling expansion the quadrupole of the polarization (i.e. $\Delta_{\text{Q}2}$) is proportional to the zeroth-order dipole. Since the zeroth-order dipole feels the Lorentz force, the polarization is also affected by the presence of large-scale magnetic fields.

3 Magnetized initial conditions for the Boltzmann hierarchy

At early times, close to the moment when initial conditions are set, the evolution equations for baryons and photons are integrated in the tight-coupling approximation. Otherwise this would represent a stiff problem owing to the largeness of the Thompson rate. Consider, first of all, the difference between the baryon velocity equation (i.e. Eq. (2.38)) and the photon velocity equation (i.e. Eq. (2.41)); the result of this manipulation is:

$$(\theta_\gamma - \theta_b)' + \frac{\epsilon'}{R_b}(1 + R_b)(\theta_\gamma - \theta_b) = k^2 \frac{\delta_\gamma}{4} + \mathcal{H}\theta_b - \frac{k^2}{4R_b}(\Omega_B - 4\sigma_B), \quad (3.1)$$

where Eq. (2.57) has been also used to express the Lorentz force in terms of Ω_B and σ_B . Owing to the presence of ϵ' , Eq. (3.1) stipulates that any initial difference in the baryon-photon velocity is quickly washed out. Consequently, at early times $\theta_\gamma \simeq \theta_b$.

Denoting by $\theta_{\gamma b}$ the common value of the photon-baryon velocity field, the corresponding evolution equation can be obtained by combining Eqs. (2.38) and (2.41) in such a way that the scattering terms exactly cancel at the price of introducing explicitly R_b i.e. the baryon-to-photon ratio of Eq. (2.22). The net result of this procedure is:

$$\theta'_{\gamma b} + \frac{\mathcal{H}R_b}{1 + R_b}\theta_{\gamma b} + \frac{\eta}{\rho_\gamma(R_b + 1)}k^2\theta_{\gamma b} = \frac{k^2}{4(1 + R_b)}\delta_\gamma + \frac{k^2(\Omega_B - 4\sigma_B)}{4(1 + R_b)}, \quad (3.2)$$

where we have also taken into account the shear viscosity contribution (proportional to η) which is responsible of the diffusion damping:

$$\eta = \frac{4}{15}\rho_\gamma\lambda_{\text{Th}}, \quad \lambda_{\text{Th}} = \frac{1}{\epsilon'}. \quad (3.3)$$

The shear viscosity term (to a given order in the tight-coupling expansion) allows for the estimate of diffusive effects. Standard considerations related to the zeroth-order in the tight coupling expansion imply that

$$\frac{1}{k_D^2} = \frac{2}{5} \int_0^\tau c_{\text{sb}}(\tau') \frac{a_0 d\tau'}{a(\tau') x_e n_e \sigma_{\text{Th}}}. \quad (3.4)$$

To second order in the tight-coupling expansion the inclusion of the polarization allows to estimate [52]:

$$\frac{1}{k_D^2} = \int_0^\tau \frac{d\tau'}{6(R_b + 1)\epsilon'} \left[\frac{16}{15} + \frac{R_b^2}{R_b + 1} \right]. \quad (3.5)$$

The factor 16/15 arises since the polarization fluctuations are taken consistently into account in the derivation. This difference is physically relevant. Grossly speaking we can indeed say that more polarization implies more anisotropy (and vice versa); more polarization implies a faster damping by diffusion. Note that k_D provides an effective ultra-violet cut-off for the magnetic energy spectra and will be used later on.

Correspondingly Eqs. (2.37) and (2.41) can be written as

$$\delta'_\gamma = \frac{2}{3}h' - \frac{4}{3}\theta_{\gamma b}, \quad \delta'_b = \frac{h'}{2} - \theta_{\gamma b}. \quad (3.6)$$

Equations (3.2) and (3.6) can be further combined to get a single equation for the density contrast of the radiation field δ_γ with the result that

$$\delta''_\gamma + \frac{\mathcal{H}R_b}{R_b + 1}\delta'_\gamma + k^2 c_{\text{sb}}^2 \delta_\gamma = \frac{2}{3} \frac{[(R_b + 1)h']'}{R_b + 1} + \frac{k^2}{3(R_b + 1)}[4\sigma_B - \Omega_B], \quad (3.7)$$

where the Silk damping has been neglected.

The same equation can be obtained by systematically expanding the brightness perturbations of the radiation field (see, in particular, Eqs. (2.80) and (2.83)) to zeroth order in the tight coupling expansion and by recalling that the precise relation between the monopole of the radiation intensity and the photon density contrast is given by $4\Delta_{I0} = \delta_\gamma$. In Eq. (3.7) the baryon-photon sound speed c_{sb} has been introduced (see Eq. (2.21)). In the absence of magnetic fields, the second source term in Eq. (3.7) vanishes. The resulting equation (in different gauges) can be again employed for the semi-analytical estimates of the temperature autocorrelations [53, 54, 55, 56, 57].

The whole Einstein-Boltzmann hierarchy will now be solved to zeroth-order in the tight-coupling expansion and for typical wavelengths larger than the Hubble radius before equality (i.e. $k\tau < 1$ for $\tau < \tau_{\text{eq}}$). The Hamiltonian constraint of Eq. (2.62) and Eq. (2.66) will first be solved. The obtained solution, parametrized in terms of a suitable number of arbitrary constants, will be inserted into the other equations. The final solution will only depend upon the spectrum of the adiabatic mode and upon the power spectra of Ω_{B} and σ_{B} . Equations (2.62) and (2.66) are solved provided:

$$\xi(k, \tau) = -2C(k) + A_\xi(k)k^2\tau^2, \quad h(k, \tau) = -C(k)k^2\tau^2 - A_h(k)k^4\tau^4, \quad (3.8)$$

$$\delta_\gamma(k, \tau) = -R_\gamma\Omega_{\text{B}}(k) - A_\gamma(k)k^2\tau^2, \quad \delta_\nu(k, \tau) = -R_\nu\Omega_{\text{B}}(k) - A_\nu(k)k^2\tau^2. \quad (3.9)$$

To lowest order in $k\tau$, $h(k, \tau)$ does not have a constant term whose presence would entail a spurious gauge mode which must be projected out by exploiting the remaining gauge freedom [38]. The compatibility of Eqs. (3.8) and (3.9) with Eqs. (2.62) and (2.66) leads to the following condition

$$3(R_\gamma A_\gamma(k) + R_\nu A_\nu(k)) = 2C(k), \quad (3.10)$$

which guarantees that Eqs. (2.62) and (2.66) are satisfied with corrections which are $\mathcal{O}(k^4\tau^2)$. In Eq. (3.10) $R_\gamma = 1 - R_\nu$ (see Eq. (2.16)). The neutrino and photon fractions arise since, prior to equality, the Hamiltonian constraint of Eq. (2.62) can be simply written, after using Eq. (2.2), as $4k^2\xi - 2\mathcal{H}h' = 3\mathcal{H}^2[R_\nu\delta_\nu + R_\gamma\delta_\gamma]$. Equation (2.66) can be also recast in a similar form.

The evolution equations of the velocity fields can be solved with a similar technique. In particular Eqs. (2.10)–(2.11) and (3.2)–(3.6) imply that

$$\theta_{\gamma\text{b}}(k, \tau) = D_{\gamma\text{b}}^{(1)}(k)k^2\tau + D_{\gamma\text{b}}^{(2)}(k)k^4\tau^3, \quad \theta_\nu(k, \tau) = D_\nu^{(1)}(k)k^2\tau + D_\nu^{(2)}(k)k^4\tau^3, \quad (3.11)$$

where the various constants must satisfy:

$$3A_\gamma(k) = 2D_{\gamma\text{b}}^{(1)}(k) + 2C(k), \quad 3A_\nu(k) = 2D_\nu^{(1)}(k) + 2C(k), \quad (3.12)$$

$$D_{\gamma\text{b}}^{(1)}(k) = \frac{R_\nu}{4}\Omega_{\text{B}}(k) - \sigma_{\text{B}}(k), \quad D_\nu^{(1)}(k) = \frac{R_\gamma}{R_\nu}\sigma_{\text{B}}(k) - \frac{R_\gamma}{4}\Omega_{\text{B}}(k). \quad (3.13)$$

The compatibility of the obtained solution with the momentum constraint of Eq. (2.63) imposes, moreover, the following pair of conditions

$$R_\nu D_\nu^{(1)}(k) + R_\gamma D_{\gamma\text{b}}^{(1)}(k) = 0, \quad R_\nu D_\nu^{(2)}(k) + R_\gamma D_{\gamma\text{b}}^{(2)}(k) + A_\xi(k) = 0. \quad (3.14)$$

The evolution equations involving the neutrino anisotropic stress (i.e. Eqs. (2.12) and (2.67)) are solved by

$$\sigma_\nu(k, \tau) = -\frac{R_\gamma}{R_\nu}\sigma_{\text{B}}(k) + A_\sigma(k)k^2\tau^2. \quad (3.15)$$

As in the previous cases there are non-trivial conditions to be satisfied and they are, in the case of Eqs. (2.12) and (2.67),

$$3[6A\xi(k) - C(k)] + 2C(k) = 6R_\nu A_\sigma(k), \quad A_\sigma(k) = \frac{2}{15}D_\nu^{(1)}(k) + \frac{2}{15}C(k) - \frac{4}{5}A_\xi(k). \quad (3.16)$$

We are left with the evolution equations of the baryon and CDM density contrasts and with the velocity field of the CDM perturbations. The solutions for these quantities, as they emerge, respectively, from Eqs. (3.6) and (2.8) are:

$$\begin{aligned} \theta_c(k, \tau) &= 0, & \delta_c(k, \tau) &= -\frac{3}{4}R_\gamma\Omega_B(k) - \frac{C(k)}{2}k^2\tau^2, \\ \delta_b(k, \tau) &= -\frac{3}{4}R_\gamma\Omega_B(k) - \frac{1}{2}\left[C(k) - \sigma_B(k) + \frac{R_\nu}{4}\Omega_B(k)\right]k^2\tau^2. \end{aligned} \quad (3.17)$$

All the compatibility conditions constraining the form of the solution can be solved, and, after some algebra, the full solution for the initial conditions of the lowest multipoles of the Einstein- Boltzmann hierarchy becomes:

$$\xi(k, \tau) = -2C(k) + \left[\frac{4R_\nu + 5}{6(4R_\nu + 15)}C(k) + \frac{R_\gamma(4\sigma_B(k) - R_\nu\Omega_B(k))}{6(4R_\nu + 15)}\right]k^2\tau^2, \quad (3.18)$$

$$\begin{aligned} h(k, \tau) &= -C(k)k^2\tau^2 - \frac{1}{36}\left[\frac{8R_\nu^2 - 14R_\nu - 75}{(2R_\nu + 25)(4R_\nu + 15)}C(k) \right. \\ &\quad \left. + \frac{R_\gamma(15 - 20R_\nu)}{10(4R_\nu + 15)(2R_\nu + 25)}(R_\nu\Omega_B(k) - 4\sigma_B(k))\right]k^4\tau^4, \end{aligned} \quad (3.19)$$

$$\delta_\gamma(k, \tau) = -R_\gamma\Omega_B(k) - \frac{2}{3}\left[C(k) - \sigma_B(k) + \frac{R_\nu}{4}\Omega_B(k)\right]k^2\tau^2, \quad (3.20)$$

$$\delta_\nu(k, \tau) = -R_\gamma\Omega_B(k) - \frac{2}{3}\left[C(k) + \frac{R_\gamma}{4R_\nu}\left(4\sigma_B(k) - R_\nu\Omega_B(k)\right)\right]k^2\tau^2, \quad (3.21)$$

$$\delta_c(k, \tau) = -\frac{3}{4}R_\gamma\Omega_B(k) - \frac{C(k)}{2}k^2\tau^2, \quad (3.22)$$

$$\delta_b(k, \tau) = -\frac{3}{4}R_\gamma\Omega_B(k) - \frac{1}{2}\left[C(k) - \sigma_B(k) + \frac{R_\nu}{4}\Omega_B(k)\right]k^2\tau^2, \quad (3.23)$$

$$\theta_{\gamma b}(k, \tau) = \left[\frac{R_\nu}{4}\Omega_B(k) - \sigma_B\right]k^2\tau - \frac{1}{36}\left[2C(k) + \frac{R_\nu\Omega_B(k) - 4\sigma_B(k)}{2}\right]k^4\tau^3, \quad (3.24)$$

$$\begin{aligned} \theta_\nu(k, \tau) &= \left[\frac{R_\gamma}{R_\nu}\sigma_B(k) - \frac{R_\gamma}{4}\Omega_B(k)\right]k^2\tau - \frac{1}{36}\left[\frac{2(4R_\nu + 23)}{4R_\nu + 15}C(k) \right. \\ &\quad \left. + \frac{R_\gamma(4R_\nu + 27)}{2R_\nu(4R_\nu + 15)}(4\sigma_B(k) - R_\nu\Omega_B(k))\right]k^4\tau^3, \end{aligned} \quad (3.25)$$

$$\theta_c(k, \tau) = 0, \quad (3.26)$$

$$\sigma_\nu(k, \tau) = -\frac{R_\gamma}{R_\nu}\sigma_B(k) + \left[\frac{4C(k)}{3(4R_\nu + 15)} + \frac{R_\gamma(4\sigma_B(k) - R_\nu\Omega_B)}{2R_\nu(4R_\nu + 15)}\right]k^2\tau^2. \quad (3.27)$$

In the limit $\Omega_B(k) \rightarrow 0$ and $\sigma_B(k) \rightarrow 0$ the solution corresponds to the usual adiabatic mode. To lowest order, in fact, we can appreciate that the non-adiabatic pressure fluctuations introduced in Eqs. (2.71) and (2.72) vanish since

$$\delta_\gamma(k, \tau) \simeq \delta_\nu(k, \tau) \simeq \frac{4}{3}\delta_c(k, \tau) \simeq \frac{4}{3}\delta_b(k, \tau). \quad (3.28)$$

The adiabatic mode is parametrized in terms of $C(k)$. The spectrum of $C(k)$ is related to the spectrum of $\mathcal{R}_*(k)$ introduced in Eq. (2.78). Equation (3.18) can be inserted into Eq. (2.73) with the result that,

to lowest order in $k\tau$, $\mathcal{R}(k) = -2C(k)$. According to Eq. (3.26), the CDM velocity field is set exactly to 0. This requirement avoids the presence of the second gauge mode (the first one was projected out by excluding the constant solution for $h(k, \tau)$). For infinitesimal diffeomorphisms (see also the Appendix) the metric fluctuations change by the Lie derivative in the direction parametrized by the two gauge parameters $\tilde{\epsilon}_0$ and $\tilde{\epsilon}$. By imposing the synchronous gauge the $\tilde{\epsilon}_0$ and $\tilde{\epsilon}$ are determined only up to two functions which are constant in time but not in space. This is the ultimate rationale for the possible persistence, in the synchronous gauge, of two spurious gauge modes. Such a possibility is avoided by gauging away the two unphysical solutions and this achieved, at a practical level, by setting $\theta_c(k, \tau) = 0$ and by requiring that $h(k, \tau)$ does not have a constant mode. A complementary way of addressing this issue is to work out the same solution in a frame where the gauge freedom is completely removed. The solution obtained in this gauge must match with the results obtained in the synchronous gauge and transformed to the new gauge. In the case of the present problem, also following previous works, it is productive to cross-check the results in the longitudinal coordinate system. The main ingredients for this analysis are reported in the Appendix where the synchronous and longitudinal solutions are explicitly connected.

The initial spectrum of the magnetic fields is encoded in Ω_B and σ_B . The spectrum of $\Omega_B(k)$ and $\sigma_B(k)$ must then be computed in terms of the spectrum of the magnetic field introduced in Eqs. (2.59) and (2.60). This is a rather lengthy calculation and here only the main steps will be outlined.

Since both $\Omega_B(\vec{x})$ and $\sigma_B(\vec{x})$ are quadratic in the magnetic field intensities (see, for instance, Eqs. (2.55) and (2.56)) their expressions in Fourier space will lead to the following two convolutions

$$\Omega_B(\vec{q}) = \frac{1}{(2\pi)^{3/2}} \frac{1}{8\pi\bar{\rho}_\gamma} \int d^3k B_i(k) B^i(\vec{q} - \vec{k}), \quad (3.29)$$

$$\sigma_B(\vec{q}) = \frac{1}{(2\pi)^{3/2}} \frac{1}{16\pi\bar{\rho}_\gamma} \int d^3k \left[\frac{3(q^j - k^j)k^i}{q^2} B_j(k) B_i(\vec{q} - \vec{k}) - B_i(\vec{q} - \vec{k}) B^i(\vec{k}) \right]. \quad (3.30)$$

The correlation functions for $\Omega_B(\vec{k})$ and $\sigma_B(\vec{k})$ are then defined as

$$\langle \Omega_B(\vec{q}) \Omega_B(\vec{p}) \rangle = \frac{2\pi^2}{q^3} \mathcal{P}_\Omega(q) \delta^{(3)}(\vec{q} + \vec{p}), \quad \langle \sigma_B(\vec{q}) \sigma_B(\vec{p}) \rangle = \frac{2\pi^2}{q^3} \mathcal{P}_\sigma(q) \delta^{(3)}(\vec{q} + \vec{p}), \quad (3.31)$$

To compute $\mathcal{P}_\Omega(q)$ and $\mathcal{P}_\sigma(q)$ in terms of the magnetic power spectra we must go through the straightforward (but rather lengthy) procedure of expressing the stochastic averages of four fields in terms of the two-point function of Eqs. (2.59) and (2.60). Then the obtained results must be integrated over the momenta. After performing the first of the previously mentioned steps we obtain

$$\mathcal{P}_\Omega(q) = \frac{q^3}{(2\pi)} \frac{1}{8\pi\bar{\rho}_\gamma} \int d^3k \frac{P_B(k)}{k^3} \frac{P_B(|\vec{q} - \vec{k}|)}{|\vec{q} - \vec{k}|^3} \left\{ 1 + \frac{[\vec{k} \cdot (\vec{q} - \vec{k})]^2}{k^2 |\vec{q} - \vec{k}|^2} \right\} \quad (3.32)$$

$$\begin{aligned} \mathcal{P}_\sigma(p) &= \frac{p^3}{(2\pi)} \frac{1}{(16\pi\bar{\rho}_\gamma)^2} \int d^3k \frac{P_B(k)}{k^3} \frac{P_B(|\vec{p} - \vec{k}|)}{|\vec{p} - \vec{k}|^3} \left\{ 1 + \frac{[\vec{k} \cdot (\vec{p} - \vec{k})]^2}{k^2 |\vec{p} - \vec{k}|^2} \right. \\ &+ \frac{6}{p^2} \left[\vec{k} \cdot (\vec{p} - \vec{k}) - \frac{[\vec{k} \cdot (\vec{p} - \vec{k})]^3}{k^2 |\vec{p} - \vec{k}|^2} \right] \\ &\left. + \frac{9}{p^4} \left[k^2 |\vec{p} - \vec{k}|^2 - 2[\vec{k} \cdot (\vec{p} - \vec{k})]^2 + \frac{[\vec{k} \cdot (\vec{p} - \vec{k})]^4}{k^2 |\vec{p} - \vec{k}|^2} \right] \right\}. \end{aligned} \quad (3.33)$$

In Eqs. (3.32) and (3.33) the notation $k = |\vec{k}|$ has been employed. To complete the calculation the angular integration and then the radial integration must be performed. The integration measure can

be written, in spherical coordinates, as $d^3k = k^2 dk d\cos\vartheta d\varphi$. The integration over φ is trivial and leads just to a factor 2π . However the integration over $d\cos\vartheta$ (between -1 and 1) is rather cumbersome (but doable in exact terms). Indeed all scalar products arising in Eqs. (3.32) and (3.33) induce a factor $\cos\vartheta$. So calling $x = \cos\vartheta$, the expressions like $|\vec{q} - \vec{k}|$ (which appear ubiquitously in Eqs. (3.32) and (3.33)) become $|\vec{q} - \vec{k}| = \sqrt{q^2 + k^2 - 2qkx}$. The combinations of all similar factors must then be integrated over x . The physically interesting region of spectra is realized when $1 < n_B < 5/2$. We will conventionally refer to this case as to the one of blue spectral indices. It is also interesting to discuss in some detail the case of red spectra (i.e. $n_B < 1$). Violet spectra (i.e. $n_B \gg 1$) are mainly constrained by the diffusion scale k_D (see Eq. (3.5)). Simplistic estimates of the Silk damping scale lead to $k_D^{-2} \simeq 0.3(a/a_{\text{dec}})^{5/2}/[\sqrt{\omega_M}\omega_b]$ Mpc². The exactly scale-invariant case leads to a logarithmically divergent power spectrum.

The magnetic power spectra are usually defined within an appropriate regularization of the magnetic energy density [30]:

$$\langle B_i(\vec{x})B^i(\vec{y}) \rangle = 2 \int d\ln k P_B(k) \frac{\sin kr}{kr} W(k), \quad r = |\vec{x} - \vec{y}|, \quad (3.34)$$

where $W(k)$ is an appropriate window function. Consider first the case of a blue spectrum. The energy density can be regularized over a typical comoving scale L (which is related to the magnetic pivot scale in Fourier space) by means of a Gaussian window function $W(k) = e^{-k^2 L^2}$. Equation (2.61) then implies:

$$B_L^2(r) = (2\pi)^{1-n_B} \mathcal{A}_B \Gamma\left(\frac{n_B-1}{2}\right) F_{11}\left(\frac{n_B-1}{2}, \frac{3}{2}, -\frac{r^2 k_L^2}{16\pi^2}\right), \quad (3.35)$$

where $F_{11}(a, b, z)$ is the Kummer confluent hypergeometric function [48, 49]. Since $\lim_{z \rightarrow 0} F_{11}(a, b, z) = 1$,

$$B_L^2 = \lim_{r \rightarrow 0} \langle B_i(\vec{x})B_j(\vec{y}) \rangle = \mathcal{A}_B^2 (2\pi)^{1-n_B} \Gamma\left(\frac{n_B-1}{2}\right). \quad (3.36)$$

In the radial integrals of Eqs. (3.32) and (3.33), \mathcal{A}_B can be traded for B_L^2 so that $\mathcal{P}_\Omega(k)$ and $\mathcal{P}_\sigma(k)$ can be written, respectively, as:

$$\mathcal{P}_\Omega(k) = \bar{\Omega}_{\text{BL}}^2 \left(\frac{k}{k_L}\right)^{2(n_B-1)} \mathcal{F}(n_B), \quad \mathcal{P}_\sigma(k) = \bar{\Omega}_{\text{BL}}^2 \left(\frac{k}{k_L}\right)^{2(n_B-1)} \mathcal{G}(n_B), \quad (3.37)$$

where

$$\bar{\Omega}_{\text{BL}} = \frac{B_L^2}{8\pi\bar{\rho}_\gamma} = 7.5 \times 10^{-9} \left(\frac{B_L}{\text{nG}}\right)^2, \quad (3.38)$$

$$\mathcal{F}(n_B) = \frac{(2\pi)^{2(n_B-1)}}{\Gamma^2\left(\frac{n_B-1}{2}\right)} \left[\frac{4(7-n_B)}{3(n_B-1)(5-2n_B)} + \frac{4}{(2n_B-5)} \left(\frac{k}{k_D}\right)^{5-2n_B} \right] \quad (3.39)$$

$$\mathcal{G}(n_B) = \frac{(2\pi)^{2(n_B-1)}}{\Gamma^2\left(\frac{n_B-1}{2}\right)} \left[\frac{n_B+29}{15(5-2n_B)(n_B-1)} + \frac{7}{5} \frac{1}{(2n_B-5)} \left(\frac{k}{k_D}\right)^{5-2n_B} \right], \quad (3.40)$$

It should be remarked that when $1 < n_B < 5/2$, we can formally send the diffusion scale to infinity (i.e. $k_D \rightarrow \infty$) and the final result will still be convergent. Consequently, as already remarked in related contexts [28] the diffusion damping only enters the case when the spectral slopes are violet (i.e. $n_B \gg 5/2$).

For $n_B < 1$ the window function appearing in Eq. (3.34) can be chosen as a simple step function $W(k) = \theta(k - k_0)$. If this is the case $\mathcal{P}_\Omega(k)$ and $\mathcal{P}_\sigma(k)$ can be formally written exactly as in Eq. (3.37) but with two slightly different pre-factors which shall be denoted by $\overline{\mathcal{F}}(n_B)$ and $\overline{\mathcal{G}}(n_B)$:

$$\mathcal{P}_\Omega(k) = \overline{\Omega}_{\text{BL}}^2 \left(\frac{k}{k_0} \right)^{2(n_B-1)} \overline{\mathcal{F}}(n_B), \quad \mathcal{P}_\sigma(k) = \overline{\Omega}_{\text{BL}}^2 \left(\frac{k}{k_0} \right)^{2(n_B-1)} \overline{\mathcal{G}}(n_B), \quad (3.41)$$

where

$$\overline{\mathcal{F}}(n_B) = \frac{16}{3} (1 - n_B)^2 \left[\frac{n_B - 7}{(n_B - 1)(2n_B - 5)} + \frac{2}{1 - n_B} \left(\frac{k_0}{k} \right)^{n_B-1} \right], \quad (3.42)$$

$$\overline{\mathcal{G}}(n_B) = (1 - n_B)^2 \left[\frac{4n_B + 116}{15(5 - 2n_B)(n_B - 1)} + \frac{8}{3} \frac{1}{1 - n_B} \left(\frac{k_0}{k} \right)^{n_B-1} \right]. \quad (3.43)$$

where k_0 is of the order of (but smaller than) the Hubble rate.

For normalization purposes it is useful to have an explicit expression of the Sachs-Wolfe plateau which includes the magnetic energy density. This estimate can be performed by solving Eq. (2.80) with the line integration method. The result of this procedure is

$$\begin{aligned} \Delta_{\text{I}}(\vec{k}, \hat{n}, \tau) &= \int_0^{\tau_0} e^{-ik\mu(\tau_0-\tau)} e^{-\epsilon(\tau, \tau_0)} \left[-\xi' + \frac{\mu^2}{2} (h' + 6\xi') \right] + \\ &\int_0^{\tau_0} e^{-ik\mu(\tau_0-\tau)} \mathcal{K}(\tau) \left[\Delta_{\text{I0}} + \mu v_b - \frac{1}{2} P_2(\mu) S_{\text{Q}} \right], \end{aligned} \quad (3.44)$$

where $\mathcal{K}(\tau)$ is the visibility function and

$$\epsilon(\tau, \tau_0) = \int_\tau^{\tau_0} \frac{a}{a_0} \sigma_{\text{Th}} n_e, \quad \mathcal{K}(\tau) = \epsilon' e^{-\epsilon(\tau, \tau_0)}. \quad (3.45)$$

The term μ^2 appearing in Eq. (3.44) can be integrated by parts and, subsequently, the visibility function can be approximated by a Dirac delta function centered at the decoupling time. Neglecting the integrated Sachs-Wolfe contribution and the Doppler term:

$$\Delta_{\text{I}}^{(\text{SW})}(\vec{k}, \hat{n}, \tau_{\text{dec}}) = \left[\frac{\delta_\gamma}{4} - \frac{(h + 6\xi)''}{2k^2} \right]_{\tau_{\text{dec}}} e^{-ik\mu\tau_0}, \quad (3.46)$$

where τ_{dec} has been neglected in comparison with τ_0 in the argument of the exponential factor. To evaluate Eq. (3.46) we need to know the value of the combination $(h + 6\xi)'$ after equality when the relevant modes have wavelengths larger than the Hubble radius. Let us notice that, for the mentioned wavelengths, Eq. (3.6) implies that $\delta'_\gamma \simeq 2h'/3$. Thus, denoting by $\delta_\gamma^{(\text{f})}$ and $\delta_\gamma^{(\text{i})}$ the final (i.e. at the decoupling) and initial (i.e. before equality) values of the density contrast we will have

$$\delta_\gamma^{(\text{f})} = \delta_\gamma^{(\text{i})} + \frac{2}{3} (h^{(\text{f})} - h^{(\text{i})}). \quad (3.47)$$

The evolution of ξ across equality can be obtained from Eqs. (2.73), (2.76) and (2.77) and it is given by solving the following equation:

$$\frac{d\xi}{d\alpha} + \frac{3\alpha + 4}{2\alpha(\alpha + 1)} \xi = \frac{4 + 3\alpha}{2\alpha(\alpha + 1)} \left[\mathcal{R}_*(k) - \frac{3R_\gamma \Omega_B(k) \alpha}{4(3\alpha + 4)} \right], \quad (3.48)$$

where $\alpha = a/a_{\text{eq}}$. Once ξ is known we can easily deduce $(h + 6\xi)'$ from Eq. (2.67) which implies (neglecting the anisotropic stress when the corresponding wavelengths are larger than the Hubble radius):

$$[(h + 6\xi)'a^2]' \simeq 2k^2 a^2 \xi. \quad (3.49)$$

The final result for the ordinary Sachs-Wolfe term can then be written as

$$\Delta_{\text{I}}^{(\text{SW})}(\vec{k}, \hat{n}, \tau_{\text{dec}}) = \left[-\frac{\mathcal{R}_*(k)}{5} + \frac{R_\gamma}{20} \Omega_{\text{B}}(k) \right] e^{-ik\mu\tau_0} \quad (3.50)$$

Expanding the plane wave in series of Legendre polynomials the $\Delta_{\ell}(k, \tau_0)$ can be easily extracted and the C_ℓ estimated with standard integration over the comoving wave-number k . The result is:

$$C_\ell^{(\text{SW})} = \left[\frac{\mathcal{A}_{\mathcal{R}}}{25} \mathcal{Z}_1(n_{\text{s}}, \ell) + \frac{1}{400} R_\gamma^2 \bar{\Omega}_{\text{B}L}^2 \mathcal{Z}_2(n_{\text{B}}, \ell) - \frac{1}{50} \sqrt{\mathcal{A}_{\mathcal{R}}} R_\gamma \bar{\Omega}_{\text{B}L} \mathcal{Z}_3(n_{\text{s}}, n_{\text{B}}, \ell) \cos \gamma_{\text{br}} \right], \quad (3.51)$$

where

$$\mathcal{Z}_1(n_{\text{s}}, \ell) = \frac{\pi^2}{4} \left(\frac{k_0}{k_{\text{p}}} \right)^{n_{\text{s}}-1} 2^{n_{\text{s}}} \frac{\Gamma(3 - n_{\text{s}}) \Gamma\left(\ell + \frac{n_{\text{s}}-1}{2}\right)}{\Gamma^2\left(2 - \frac{n_{\text{s}}}{2}\right) \Gamma\left(\ell + \frac{5}{2} - \frac{n_{\text{s}}}{2}\right)}, \quad (3.52)$$

$$\mathcal{Z}_2(n_{\text{B}}, \ell) = \frac{\pi^2}{2} 2^{2(n_{\text{B}}-1)} \mathcal{F}(n_{\text{B}}) \left(\frac{k_0}{k_{\text{L}}} \right)^{2(n_{\text{B}}-1)} \frac{\Gamma(4 - 2n_{\text{B}}) \Gamma(\ell + n_{\text{B}} - 1)}{\Gamma^2\left(\frac{5}{2} - n_{\text{B}}\right) \Gamma(\ell + 3 - n_{\text{B}})}, \quad (3.53)$$

$$\begin{aligned} \mathcal{Z}_3(n_{\text{s}}, n_{\text{B}}, \ell) &= \frac{\pi^2}{4} 2^{n_{\text{B}}-1} 2^{\frac{n_{\text{s}}+1}{2}} \sqrt{\mathcal{F}(n_{\text{B}})} \left(\frac{k_0}{k_{\text{L}}} \right)^{n_{\text{B}}-1} \left(\frac{k_0}{k_{\text{p}}} \right)^{\frac{n_{\text{s}}+1}{2}} \\ &\times \frac{\Gamma\left(\frac{7}{2} - n_{\text{B}} - \frac{n_{\text{s}}}{2}\right) \Gamma\left(\ell + \frac{n_{\text{B}}}{2} + \frac{n_{\text{s}}}{4} - \frac{3}{4}\right)}{\Gamma^2\left(\frac{9}{4} - \frac{n_{\text{B}}}{2} - \frac{n_{\text{s}}}{4}\right) \Gamma\left(\frac{11}{4} + \ell - \frac{n_{\text{B}}}{2} - \frac{n_{\text{s}}}{4}\right)}. \end{aligned} \quad (3.54)$$

In Eq. (3.54) γ_{br} is the correlation angle that has been included to keep the expressions as general as possible. In what follows the main focus will however be on the case where the adiabatic mode of curvature perturbations is not correlated with the magnetized contribution (i.e. $\gamma_{\text{br}} = \pi/2$). Note, however, that if $\cos \gamma_{\text{br}} > 0$ then the cross-correlation between the adiabatic component and the magnetic component will lower the Sachs-Wolfe plateau allowing for a magnetized contribution which is comparatively larger than in the case where $\gamma_{\text{br}} = \pi/2$. We leave this possibility for future studies [50].

4 Magnetized temperature autocorrelations

In Fig. 1 the results of the numerical integration are illustrated in terms of the temperature autocorrelations. The parameters are fixed to the best fit of the WMAP data alone implying that the value of the scalar spectral index is $n_{\text{s}} = 0.958$. The full set of cosmological parameters used to compute the models in Fig. 1 is given as follows⁹:

$$(\Omega_{\text{b}0}, \Omega_{\text{c}0}, \Omega_{\Lambda}, h_0, n_{\text{s}}, \tau) = (0.042, 0.198, 0.76, 0.732, 0.958, 0.089). \quad (4.1)$$

⁹Consistently with our notations we should denote with ϵ_{re} the optical depth to reionization which is conventionally denoted by τ and which we use to indicate the conformal time. However, since in the present and in the following sections the optical depth and the conformal time coordinate are never mentioned together, we will stick to the conventional terminology and denote with τ the optical depth.

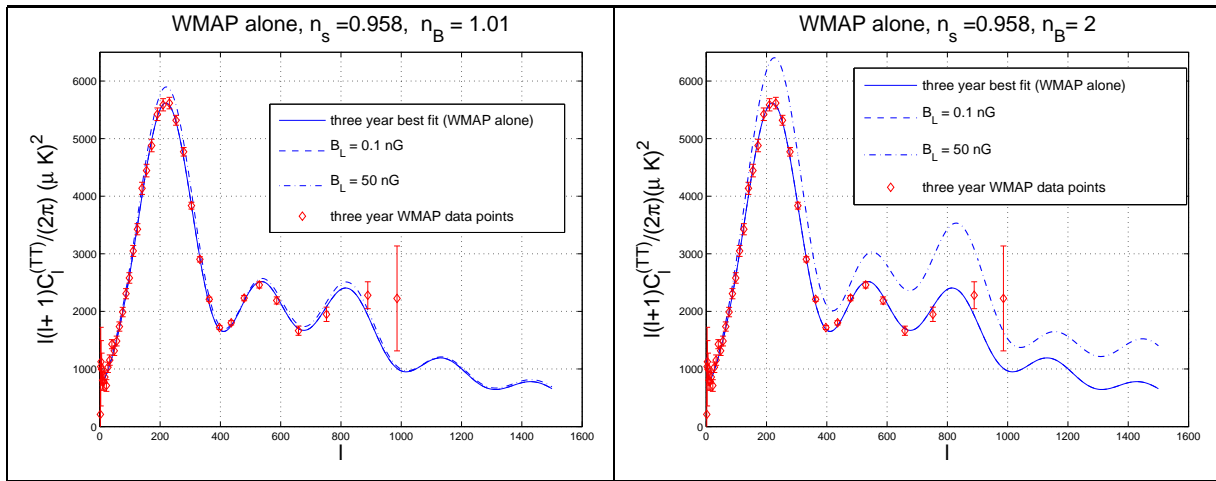


Figure 1: The temperature autocorrelations for blue magnetic spectral indices are compared with the best fit model arising from the WMAP alone analyzed in terms of a pure Λ CDM model with no tensors. The value of the magnetic pivot scale is $k_L = 1 \text{ Mpc}^{-1}$.

Moreover the tensors are absent from the fit and $R_\nu = 0.408$ (i.e., according to Eq. (2.16), $N_\nu = 3.04$). In Fig. 1 (full curve in both plots) the $C_\ell^{(TT)}$ are illustrated for the best fit parameters reported in Eq. (4.1). The magnetic spectral indices are, in both cases blue, i.e., according to the terminology of the previous section, $1 < n_B < 5/2$. With the dashed line the magnetic fields corresponding to $B_L = 0.1 \text{ nG}$ is reported. The dashed curve cannot be distinguished from the best fit curve. If the regularized magnetic field intensity is $B_L \leq \mathcal{O}(0.1 \text{ nG})$, then the difference of the TT correlations (as well as the EE and TE correlations) with respect to the three year best fit is below the accuracy of the code. The latter statement depends, of course, on the spectral index and on the range of multipoles. Indeed, as argued in Section 6, the large-multipole region (i.e. $\ell \gg 1500$) is more sensitive to regularized fields of nG strengths.

The dot-dashed curve denotes, in both plots, the temperature autocorrelations computed in the case $B_L = 50 \text{ nG}$. The results illustrated in Fig. 1 are qualitatively similar for different choices of the parameters close to the best fit values. The inclusion of a magnetized background has a threefold effect on the temperature autocorrelations. The height of the first peak gets increased. The second peak is distorted and it eventually turns into a hump for sufficiently large values of B_L (or of n_B). The third peak is, at the same time, distorted and raised. In Fig. 1 as we move from the plot at the left to the plot at the right the spectral index increases. The increase of the spectral slope entails also an increase in the distortions. The latter trend, however, is not monotonic at least in the case of the first acoustic peak. A more thorough illustration of this feature will be provided in Section 6. It should be borne in mind that, within the conventions established in Section 3 the scale-invariant limit of the magnetic power spectra is realized for $n_B \rightarrow 1$. In analog terms, the Harrison-Zeldovich limit for the power spectrum of curvature perturbations occurs when $n_s \rightarrow 1$.

The features illustrated in Fig. 1 and scrutinized in the previous paragraph do not depend upon the data sets. The same qualitative patterns can be observed if the pivotal model is taken to be the best fit inferred from the combination of the WMAP data with all the other data. In this case the central values of the cosmological parameters are slightly changed [11, 12, 13] according to:

$$(\Omega_{b0}, \Omega_{c0}, \Omega_\Lambda, h_0, n_s, \tau) = (0.044, 0.223, 0.733, 0.704, 0.947, 0.073). \quad (4.2)$$

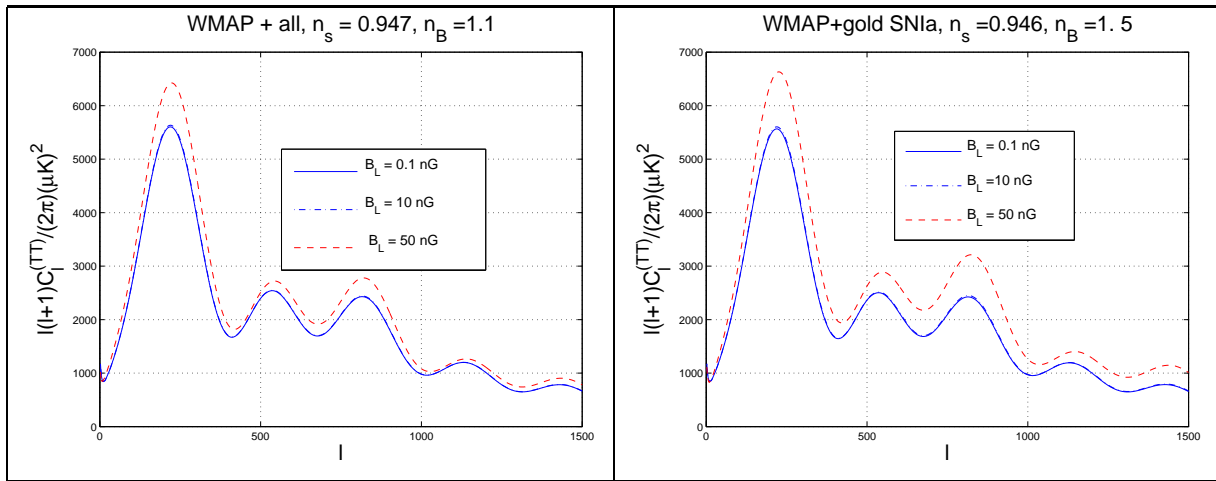


Figure 2: The temperature autocorrelations for blue magnetic spectral indices. In the plot at the left the cosmological parameters are fixed to the central values of the best fit when the WMAP data are combined with all the cosmological data sets (see Eq. (4.2)). In the plot at the right the cosmological parameters are fixed to the central values of the best fit when the WMAP data are combined with the gold sample of type Ia supernovae (see Eq. (4.3)). As in Fig. 1 the pivotal model is Λ CDM scenario with no tensors. The value of the magnetic pivot scale is $k_L = 1 \text{ Mpc}^{-1}$.

By fitting the WMAP data with the ones of the gold sample of type Ia supernovae [20] the central values of the cosmological parameters are yet a bit different from the ones reported in Eqs. (4.1) and (4.2):

$$(\Omega_{b0}, \Omega_{c0}, \Omega_{\Lambda}, h_0, n_s, \tau) = (0.045, 0.231, 0.724, 0.701, 0.946, 0.079). \quad (4.3)$$

In Fig. 2 the temperature autocorrelations are computed when the cosmological parameters are fixed as in Eq. (4.2). As the magnetic field strength increases from 10 to 50 nG the distortion patterns already illustrated in Fig. 1 become more pronounced. By comparing Figs. 1 and 2 the same distortion patterns can be observed. In Fig. 2 the spectral tilt increases from the left to the right plot. As in Fig. 1, also in Fig. 2 the plot at the left is close to the scale-invariant limit of the magnetic power spectrum while the plot at the right illustrates a spectral slope which is bluer.

The distortion patterns arising in Figs. 1 and 2 have a semi-analytical interpretation. In [33] the effects of magnetic fields on the temperature autocorrelations have been discussed in a semi-analytical perspective and for blue spectral indices (i.e. $1 < n_B < 5/2$). A consistent use of the tight-coupling approximation allowed for the estimate of the $C_{\ell}^{(TT)}$ at low multipoles (i.e. $\ell < 30$) and also at large multipoles (i.e. $\ell > 100$). Using the large-order expansion of the spherical Bessel functions (and of their derivatives) the shape of the TT correlations has been reduced to the numerical calculation of four integrals [33]. The semi-analytical approach described in [33] seems, a posteriori, rather brutal. Nonetheless it is amusing that the essential patterns of the distortions in the acoustic region have been correctly captured.

The Doppler region is sensitive to the relative phases and amplitudes of the monopole and dipole terms of the brightness perturbations. The contribution of the Lorentz force provides an extra source to the monopole equation (see Eq. (3.7)). A computable difference in the relative amplitudes of the monopole and dipole terms then arises also analytically and it is reflected in the overall distortion. The reasonable results obtainable within the tight-coupling expansion (improved to second order)

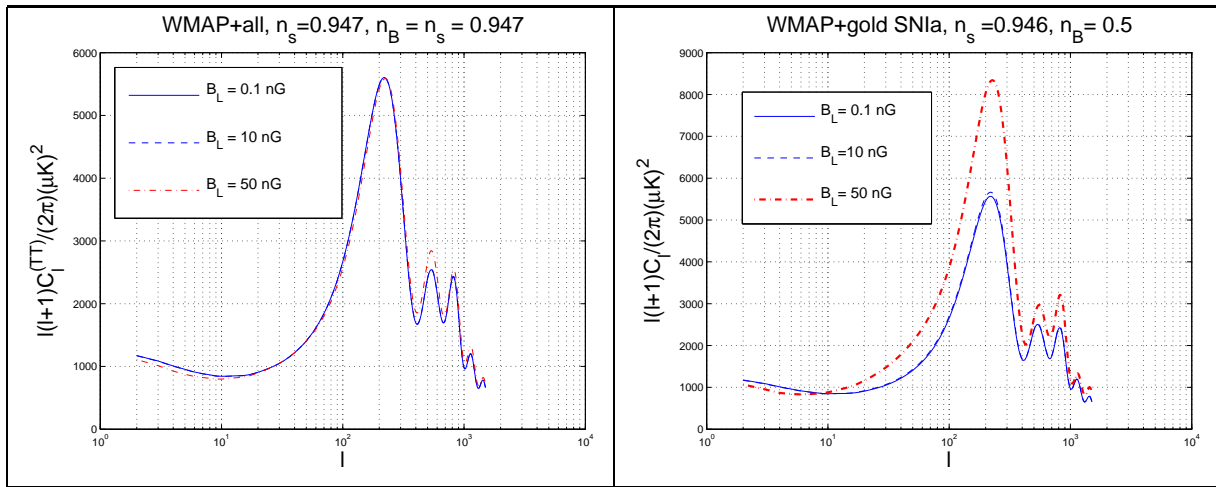


Figure 3: The temperature autocorrelations are illustrated in the case of red tilt. The values of the cosmological parameters in the left and right plots have been fixed, respectively, as in Eqs. (4.2) and (4.3).

represent a powerful cross-check for the consistency both of the numerical approach and of the semi-analytical calculation. In spite of the encouraging agreement of the numerical results with the semi-analytical evaluations, a weaker dependence upon the amplitude of the magnetic fields has to be admitted. Indeed, the reionization effects have been neglected in [33] and the recombination has been treated within a Gaussian parametrization of the visibility function. Furthermore, always in [33], the overall amplitude of the angular power spectrum was determined by matching the low- ℓ regime with the Doppler regime where the Bessel functions have been basically replaced with their asymptotic expressions for $\ell \gg 1$. Numerically these approximations have been dropped.

The range of spectral indices $1 < n_B < 5/2$, on a theoretical ground, is well motivated. The two-point function of the magnetic fields decreases, in this case at large distances. The diffusive effects are negligible since, as explained in the previous section, the two-point functions of the energy density (and of the Lorentz force) is insensitive, in this case, to the ultra-violet cut-off. Finally various magnetogenesis models predict this kind of spectra¹⁰.

The last motivation, however, is just accidental. The true question behind these considerations is slightly different and can be phrased by asking: which is the spectrum of magnetic fields at the onset of gravitational collapse of the protogalaxy? As we can in principle measure the matter power spectrum it would not be insane to think that, in a future, also the magnetic power spectra of different objects could be measured. Indeed there are attempts to characterize, for instance, the present features of our galactic magnetic field in terms of an appropriate power spectrum [59]. In a related perspective one could observe that it is equally plausible to study the mean-squared fluctuation of the Faraday Rotation Measure (RM), as it was proposed in Refs. [60, 61]. One of the key projects of the radio-astronomy community is the celebrated Square Kilometer Array (SKA)¹¹. This instrument will allow to

¹⁰See, for instance, [9] and [30] for some reviews on this subject. It would be impossible to refer to all the attempts along this direction. For recent results see [58] and references therein. As specifically discussed in the introduction, the purpose here is not to endorse a particular model but to develop the tools which will allow to assess the primordial nature of the magnetic field. In this sense the goal of the present analysis is more modest.

¹¹The collecting area of the instrument, as the name suggest, will be of 10^6 m^2 . The specifications for the SKA require an angular resolution of 0.1 arcsec at 1.4 GHz, a frequency capability of 0.1–25 GHz, and a field of view of at

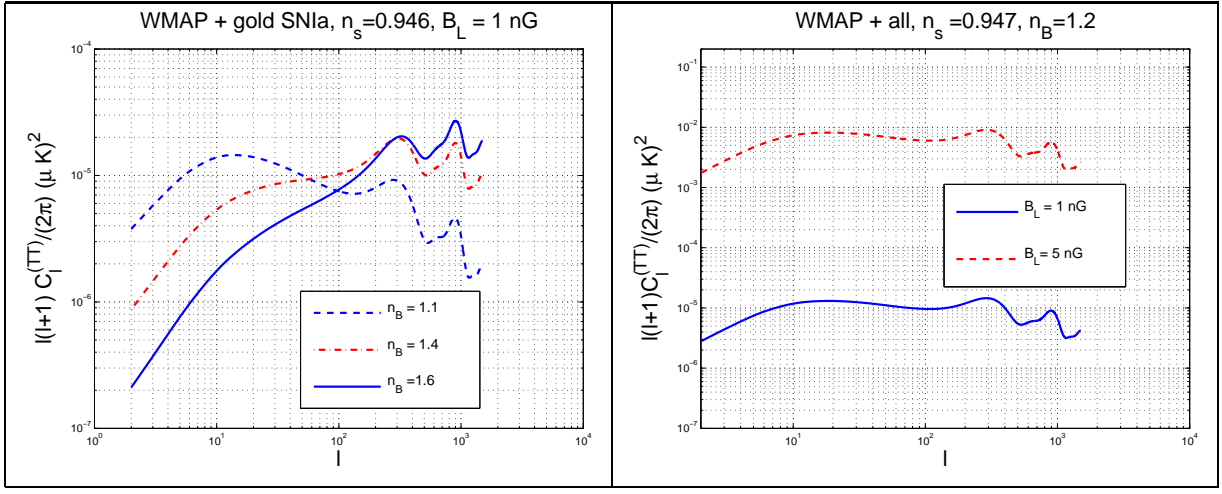


Figure 4: The temperature autocorrelations are illustrated in the case of vanishing adiabatic mode for fixed magnetic field strength (plot at the left) and for fixed magnetic spectral index (plot at the right). The magnetic pivot scale is taken to be $k_L = 1\text{Mpc}^{-1}$ and the other values of the cosmological parameters are fixed to their best fit values as in Eq. (4.2) (plot at the left) and as in Eq. (4.3) (plot at the right).

obtain full sky survey of the RM and, in that context, it will be even more plausible to collect valuable informations on the magnetic power spectra at large scales. These measurements, even if feasible in the future, will not provide direct indications on the protogalactic field but rather on the present field. Still it is not excluded that the morphological features of the observed field could be connected with the protogalactic features. If the magnetic field does not flip its sign from one spiral arm to the other, then a strong dynamo action can be suspected [64]. In the opposite case the magnetic field of spiral galaxies should be primordial i.e. present already at the onset of gravitational collapse. An excellent review on the evidence of magnetism in nearby galaxies can be found in [65]. In the model-independent approach followed in the present paper it is natural to ask what happens if the magnetic power spectra have a red tilt. In Fig. 3 (left plot) the spectral tilts of the magnetic power spectrum and of the spectrum of curvature perturbations coincide. In other words $n_s = n_B = 0.947 < 1$. The specific figure (i.e. 0.947) is dictated by the adoption, as fiducial set of data, of the best fit to the WMAP data combined with all the other data (see Eq. (4.2) and also the titles of the plots in Fig. 3). In the plot at the right of Fig. 3 the spectral indices of the magnetic energy density and of the anisotropic stress decreases (i.e. $n_B = 0.5 \ll n_s$). So we can say that, in Fig. 3 the magnetic spectral index is redder at the right than at the left. The two plots in Fig. 3 have been presented in semi-logarithmic coordinates and this choice allows to scrutinize in more depth the main feature associated with red spectral indices: as the spectral index becomes redder, a systematic decrease of the low multipoles is observed. This trend has been investigated with other examples (which will not be reported for reasons of space). The conclusion of this analysis is that, indeed, red spectra can lead to a lower quadrupole and, only apparently, improve the agreement with the data. We say *only apparently* because every time the TT correlation diminishes at low multipoles, the first pair of acoustic peaks is raised and distorted to an

least 1deg^2 at 1.4 GHz [62, 63]. The number of independent beams is expected to be larger than 4 and the number of instantaneous pencil beams will be roughly 100 with a maximum primary beam separation of about 100 deg at low frequencies (becoming 1 deg at high frequencies, i.e. of the order of 1 GHz). These specifications will probably allow full sky surveys of Faraday Rotation.

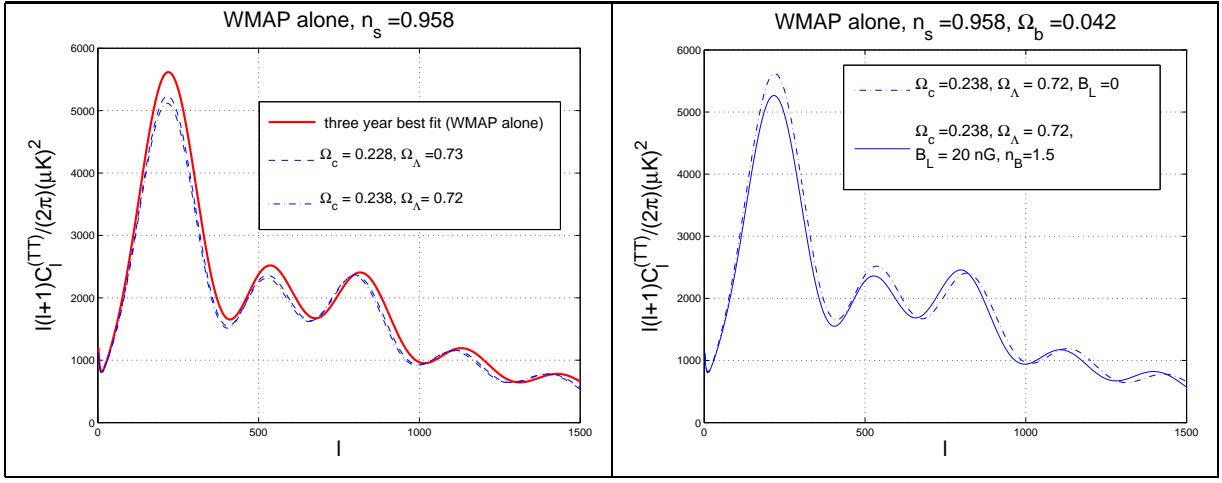


Figure 5: The effect of the magnetic fields is illustrated in the case when the CDM fraction is increased by enforcing the spatial flatness and when the baryonic fraction is kept fixed to the best fit value.

unacceptable degree. This aspect can be appreciated, in a rather extreme case, in the plot at the right of Fig. 3. For $B_L = 50$ nG the low multipoles would indeed represent better the experimental points. However, the Doppler peak explodes to, roughly, $9000(\mu\text{K})^2$.

When the spectra have a red tilt the magnetic pivot scale coincides effectively with the infra-red cut-off of the spectrum. If the cut-off is as large as the present Hubble patch the magnetic field acquires, for practical purposes a preferred direction. One could be tempted to say that this offers an explanation of the lower value of the quadrupole. Indeed various proposals have been put forward to explain the quadrupole with a specific anisotropic model falling in one of the Bianchi classes. The consistency of our numerical approach shows, however, that these kinds of red spectra lowering the quadrupole are simply pathological. Indeed, as it appears from Fig. 3, red spectral slopes lowering the quadrupole and spontaneously breaking spatial isotropy are not consistent at higher multipoles. We suspect that current attempts of justifying the quadrupole anomaly based on anisotropic models would simply fail when confronted with the higher multipoles. The considerations reported here are a first quantitative indication in this direction. It would be interesting to pursue this analysis in further detail [50]. The quadrupole anomaly is probably better addressed in the framework of pre-inflationary initial conditions such as the ones discussed in [66, 67] where the low value of the quadrupole is attributed to a fast-roll phase.

The final comment in connection with red spectra deals with regularized magnetic field of regularized amplitude much smaller than the nG. In both plots of Fig. 3 the case of $B_L = 0.1$ nG cannot be distinguished from the corresponding best fit model. The latter observation suggests that weak magnetic fields (i.e. $B_L \simeq \mathcal{O}(0.1 \text{ nG})$) with red tilt are not incompatible with current data on the TT correlations.

If the adiabatic mode of primeval origin is switched to zero, we can expect, on the basis of purely analytical considerations, that the typical amplitude of the temperature autocorrelations will be vanishingly small to begin with. Indeed, the overall amplitude will not be controlled by the power spectrum of the adiabatic mode but by the power spectrum of the magnetic energy density, i.e. $\mathcal{P}_\Omega(k)$. The amplitude of the adiabatic power spectrum evaluated at the pivot scale k_p is of the order of 10^{-9} . The amplitude of $\mathcal{P}_\Omega(k)$, evaluated at the magnetic pivot scale k_L goes as $\bar{\Omega}_{BL}^2$ which is $\mathcal{O}(10^{-18})$ for $B_L \simeq \text{nG}$.

Consequently if the adiabatic contribution is switched off we will expect that the temperature auto-correlations will be about 9 orders of magnitude smaller than in the case where the adiabatic mode was present. This means that while in the case of, for instance, Fig. 1 $\ell(\ell+1)C_\ell^{(\text{TT})}/(2\pi) \simeq 10^3(\mu\text{K})^2$, when the adiabatic mode is switched to zero $\ell(\ell+1)C_\ell^{(\text{TT})}/(2\pi) \simeq 10^{-6}(\mu\text{K})^2$.

In Fig. 4 the theoretical expectations are confirmed by the numerical results. In the plot at the right $B_L = 1\text{ nG}$. For different values of the spectral indices the TT correlation exhibit a humpy profile in the acoustic region. This point is also stressed in the right plot of Fig. 4 where for fixed n_B the magnetic field strength is enhanced from 1 nG to 5 nG. This entails an increase of the temperature autocorrelations of a factor 6×10^2 which fits with our expectation which would be, in this case, (5)⁴. According to Fig. 1 the case $B_L = 50\text{ nG}$ is already excluded by the present data and for the corresponding values of the spectral index. This observation helps along two opposite directions. The nature of the distortion induced by the magnetic fields seems to be hard to reproduce by varying the standard CMB parameters. For instance it is known that by lowering ω_b the height of the peaks diminishes. Similar effects (but with a different quantitative impact) are observed when ω_c increases (always enforcing the flatness of the model). None of these two effects distorts the peaks as in the case of magnetic fields. One can also think that by adding spatial curvature and by either decreasing ω_b or increasing ω_c the effects of the magnetic fields can be appropriately mimicked. However, in the case of the magnetic fields not only the first peak increases but also the ratio of the second to the first peak is modified. The shift in the position of the peaks is much more severe in non-flat models than in the case of nG magnetic fields.

In Fig. 5 (plot at the left) the baryonic fraction Ω_{b0} has been fixed to the best fit value of the WMAP data alone (see Eq. (4.1)). The CDM contribution has then been increased (by always keeping the model flat). In the right plot we took the most extreme model illustrated in the left plot (i.e. the one labeled by the dot-dashed line) and compared it with the same model where, however the magnetic field is included. This shows that the kind of correlated distortion induced by the magnetic fields cannot be simply reduced to an increase of the peaks (see also Section 6 for a more extended scrutiny of this statement). We analyzed the characteristic shapes obtainable by changing also other parameters as the Hubble rate and, also in that case, the magnetic fields induce distortions which cannot be mimicked by known shape effects. Under certain circumstances, a slight increase in the CDM fraction (less extreme than those illustrated in Fig. 5) can be compensated by the presence of a minute magnetized background.

This type of considerations bring up naturally the need of including the magnetic fields as an extra set of parameters in the current strategies of data analysis [25]. In its simplest realization the magnetized ΛCDM paradigm entails the inclusion of two new parameters, i.e. the magnetic spectral index and the amplitude of the regularized field. It cannot be excluded, in other words, that a combined action of different effects will be compensated by a magnetic field leading, ultimately, to a better fit. The accuracy of forthcoming data (see also Section 6) seems to suggest that we will soon be sensitive to nG magnetic fields and, then, global strategies of parameter extraction will allow either to confirm the ΛCDM paradigm or to improve it.

A handy parallel can be drawn with a slightly different physical case which however bears some analogy with the one discussed here. A commonly employed approach to the initial conditions is the one we could define as model-independent (see, for instance, [51, 68]). When analyzing cosmological data a very interesting question is to know if the data allow for a sizable non-adiabatic component. It is by now well established how to constrain the CDM-isocurvature mode [69, 70]. This analysis

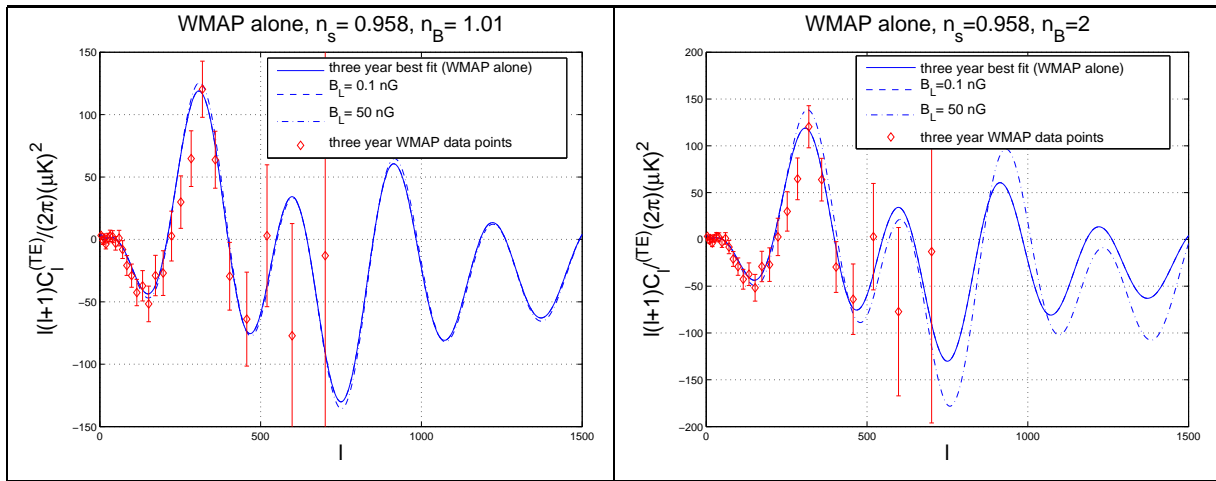


Figure 6: The magnetized TE correlations are illustrated for different values of the spectral indices and different values of the magnetic field intensities. The fiducial set of the cosmological parameters is the one of Eq. (4.1).

entails, in the simplest case, the addition of two extra-parameters, i.e. the amplitude and spectral index of the non-adiabatic mode. However there could be even more complicated situations where a cross-correlation term is present. This term parametrizes a possible correlation between the adiabatic and the non-adiabatic components and typically leads to further parameters. Recently interesting results have been reported in this context. For instance it has been shown that indeed the addition of an adiabatic component with blue spectrum may improve the global fits of cosmological parameters [71]. The situation described in the case of the isocurvature modes is similar to what happens in the case of large-scale magnetic fields with the crucial difference that, in the present case, not only the initial conditions but also the dynamics is affected by the addition of stochastic magnetic fields. As customarily done, for other parameters, it will be appropriate to include the magnetic fields when confronting all the cosmological data sets. This idea will allow to set bounds and compare fits in a way which is less brutal than the one sometimes employed when dealing with large-scale magnetic fields. The numerical approach developed and applied in the present study is the first step in this direction which we plan to investigate thoroughly in the near future [50].

Always in connection with the isocurvature modes we wish to stress that large-scale magnetic fields can be included also in the case when the initial conditions are not predominantly adiabatic but rather obtained as a mixture of adiabatic and non-adiabatic components. In this study, for reasons of space, we just focused on the magnetized adiabatic mode. It is therefore possible to study, with our approach, all the usual situations encountered in conventional CMB calculations [50].

5 Polarization correlations and cross-correlations

The TE cross-correlations are probably the strongest indicator of the adiabatic nature of the CMB initial conditions. Indeed, in the adiabatic case, the $C_l^{(TE)}$ shows a characteristic anticorrelation peak for $\ell \simeq (3/4)\ell_{\text{Doppler}} \simeq 150$ where ℓ_{Doppler} denotes the observed position of the Doppler peak [14, 32]. The relation between Doppler and anticorrelation peaks is a distinctive feature of the adiabaticity of the fluctuations prior to recombination. The polarization observations are therefore a rather sensitive

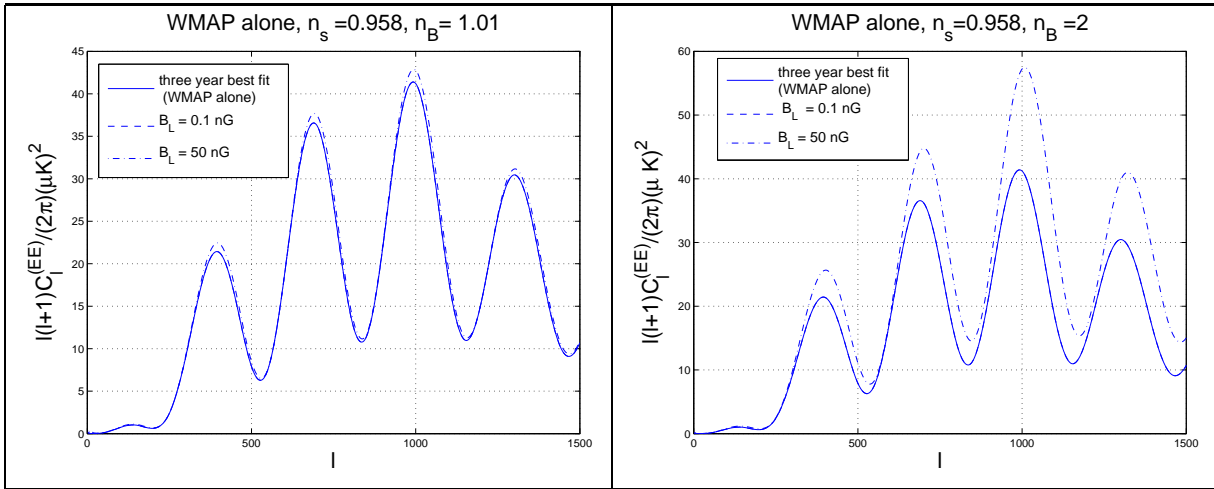


Figure 7: The magnetized EE correlations for blue values of the magnetic spectral tilt. The cosmological parameters are the same as in Fig. 6.

tool which can be used to scrutinize the possible contribution of a magnetized component. At the moment various experiments reported a positive detection of the EE and TE correlations. Besides the three year results of the WMAP collaboration [12] there are, at the moment, the three year data of the DASI experiment [72], the CAPMAP results [73], the (almost) three year results of CBI [74] and the preliminary results of QUAD [75]. In the present version of the code the polarization correlations and cross-correlations (i.e EE and TE power spectra) can be explicitly computed since consistent initial conditions have been given for the whole Boltzmann hierarchy. The magnetic field can have two distinct effects on the CMB polarization. Since gravitating magnetic fields modify the structure of the adiabatic mode and of the evolution of the baryon-photon fluid, the TE and EE angular power spectra will be different. The second effect would be due to the presence of a Faraday rotation term which would couple the evolution equations for the two brightness perturbations which are sensitive to polarization. In the language of Eqs. (2.81) and (2.82) this term would couple the U and Q Stokes parameters producing, ultimately, a rotation of the polarization plane of the CMB. The Faraday coupling can be easily included if the magnetic field is uniform [76]. In the case of stochastic magnetic field this calculation has never been done. There are certainly semi-analytical attempts in this direction (see, for instance, [77, 78, 79]). However, the main problem with these calculations is that they assume that the magnetic fields only rotate the polarization without entering in any other place of the evolution equations. There are, on the contrary, reasons to believe that, for a stochastic field, the two effects can be equally important¹². In this discussion we will not include the Faraday rotation term by a uniform field since this would break explicitly the spatial isotropy and concentrate on the numerical solution when the magnetic fields are consistently introduced in the initial conditions and in all the other evolution equations, as it was done for the TT correlations in the previous section.

In Fig. 6 the TE correlations are illustrated for the case of blue magnetic spectral indices $1 < n_B < 5/2$. The parameters used in the calculation are exactly the ones employed in Fig. 1. If the magnetic field is of the order of 0.1 nG the magnetized TE correlations cannot be distinguished from the three

¹²In nearly all Faraday rotation studies it is assumed that the description of the plasma is given in terms of a single fluid. This assumption is not correct [80]. Indeed Faraday rotation requires necessarily a kinetic treatment (or at least a two fluid treatment). We are investigating the possibility within our numerical approach [50].

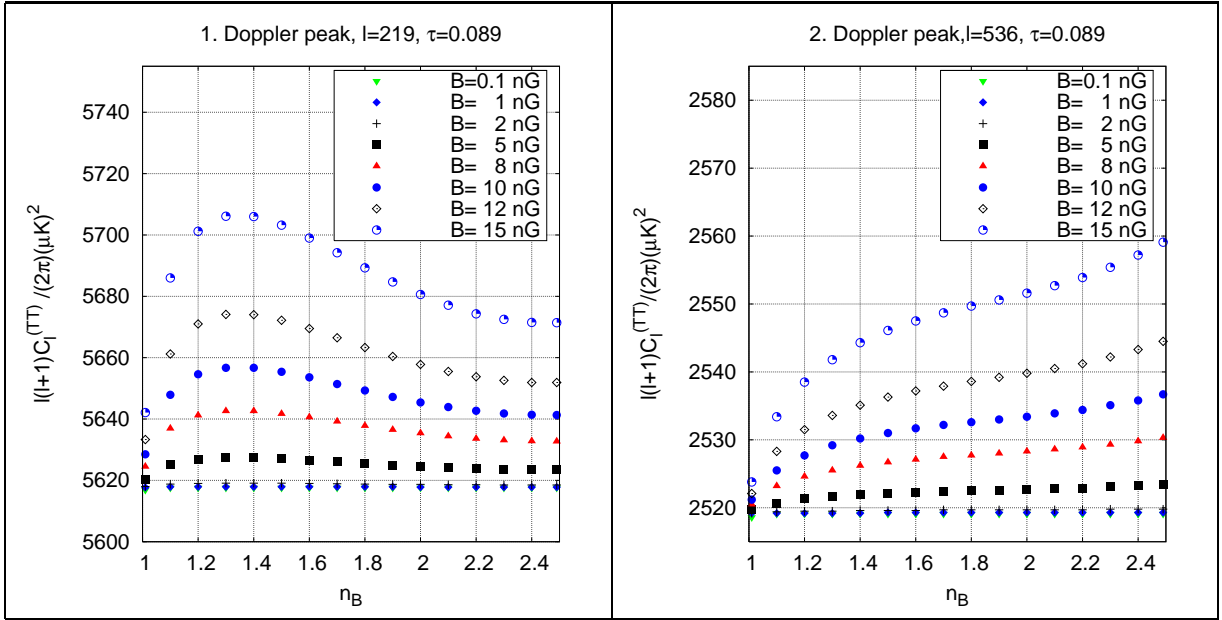


Figure 8: The height of the first and second peaks for different values of the magnetic field intensity as a function of the magnetic spectral index. The other cosmological parameters have been fixed as in Eq. (4.1).

year best fit of the WMAP data. Unlike the case of the temperature autocorrelations (where the position of the Doppler peak cannot be moved by a stochastic magnetic field) there is an observable shift of the second and third (correlation) peaks of the TE spectra. This distortion also entails a shift of the position of the corresponding peaks. A similar effect can be observed in the magnetized EE correlations which are reported in Fig. 7. Also in this case the peaks are raised and partially shifted. Figures 6 and 7 show, a posteriori, that the magnetic fields also affect the polarization observables even *without* a Faraday rotation term. This observation supports our previous statements. The physical reason of the obtained result can be understood very simply. To zeroth-order in the tight-coupling expansion, the magnetic field affects the dipole of the brightness perturbation for the intensity. Always to zeroth order, this contribution is reflected in a further source term for the monopole. But both the TE and EE power spectra arise to first-order in the tight-coupling expansion and are proportional to the first-order dipole through a term which is, up to a numerical factor, k/ϵ' [32]. This shows why we also get an effect on the polarization observables even if the Faraday rotation term is absent.

The results obtained so far show that it is possible to obtain accurate estimates of the temperature autocorrelations and of the polarization correlations also in the presence of a magnetized background. Conventional CMB calculations have a high level of accuracy and this is due, both, to the precise understanding of the initial conditions and to the thorough comprehension of the dynamics. At the moment, it is possible to achieve the same level of accuracy also when a magnetized background is included.

6 Waiting for Planck

The Planck explorer satellite [22] will provide high precision measurements of the cosmic microwave background. In view of this exciting time the quantitative trends illustrated in Sections 4 and 5

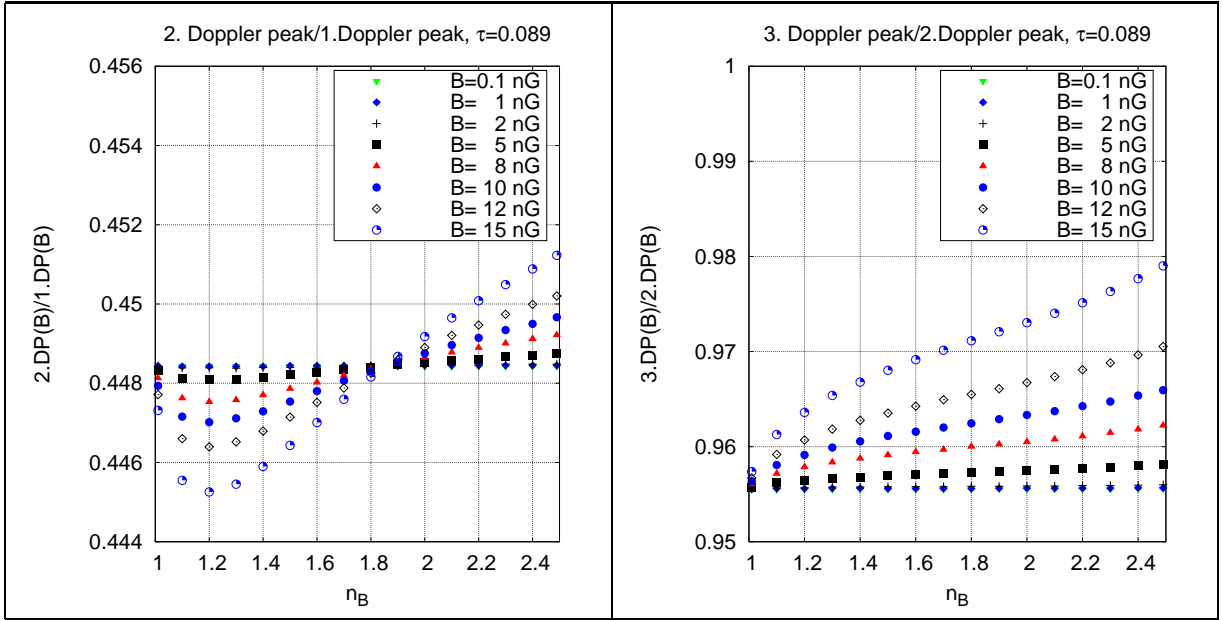


Figure 9: The ratio of the heights of the second to the first peak (plot at the left) and of the heights of the third to the first peak (plot at the right). The parameters are fixed as in Fig. 8.

will now be scrutinized in more depth. The Doppler peaks are both distorted and increased. For $2 < \ell < 2500$ the extrapolated best fit to the WMAP data alone predicts, at different locations, 7 acoustic peaks. The heights and shapes of the 7 peaks have been monitored for different values of the magnetic field intensity and of the magnetic spectral index. For reasons of space we will just focus on the first and second and on the sixth and seventh. This will suffice for the quantitative trend we wish to illustrate.

In Fig. 8 the height of the first peak is reported for different values of the regularized magnetic field, as a function of the magnetic spectral index. Note that in all the figures from Fig. 8 to 12 the title of each plot labels the peak. So, for instance, the notation “1.Doppler peak” means that the corresponding plot refers to the first Doppler peak.

The maximal increase of the acoustic peaks always arises for intermediate spectral tilts. The TT correlations are not only shifted upwards but they are also distorted: this is evident from Fig. 9 where we illustrate, respectively, the ratio of the second peak to the first (plot at the left) and the ratio of the third peak to the first. From the left plot of Fig. 9 it is clear that an increase in the spectral index entails, for $n_B < 1.8$, a decrease of the height of the second peak in comparison with the first. When $n_B > 1.8$ the opposite behaviour is observed. For a given value of the magnetic field the correlated distortion of the first peak is an effect of the order of few percent (as it can be argued from the corresponding plots). As we reach into the region $\ell > 1500$ the effect becomes more pronounced especially for the seventh peak. While the first peak is not sensitive to a nG magnetic field, the seventh peak can be a reasonable indicator of the presence of large-scale magnetic fields in the nG range. This aspect is illustrated in Fig. 10 in the cases of the sixth and seventh peaks. From the plot at the right, for instance, a 15 nG field has a 10 percent effect on the shift. The precise value depends on the spectral index, as it can be argued from Fig. 10.

The observed correlated distortion is also visible in the case of the TE angular power spectra. In Fig. 11 the first anticorrelation peak (plot at the left) is compared with the first correlation peak (plot

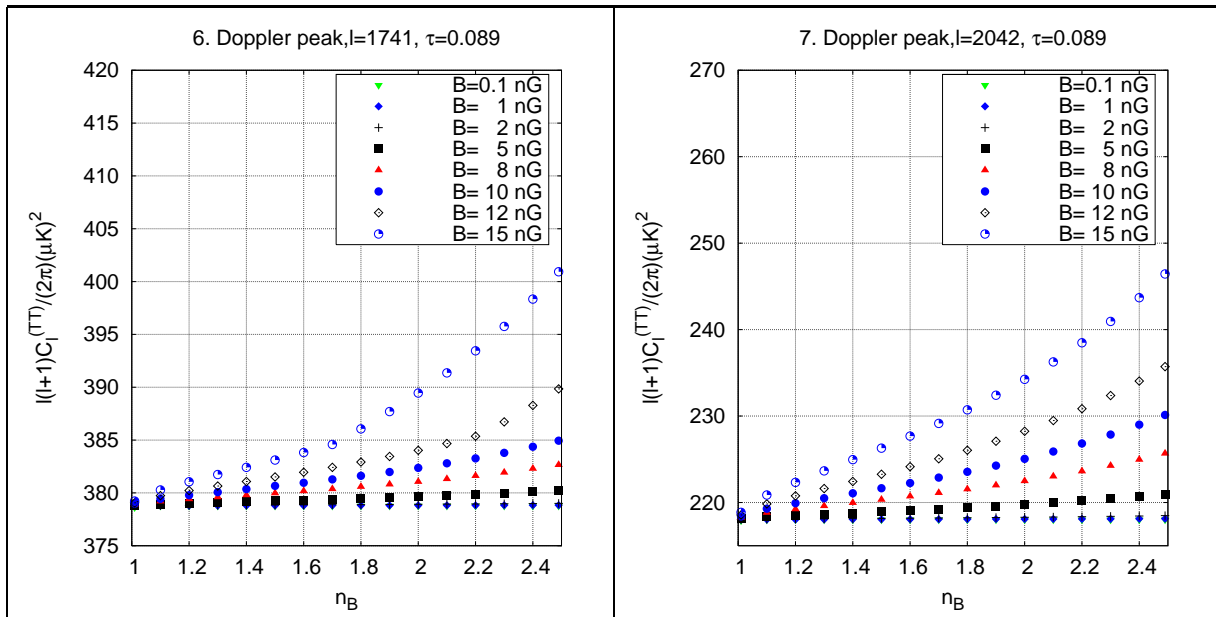


Figure 10: The heights of the sixth (plot at the left) and of the seventh (plot at the right) Doppler peaks is illustrated for different values of the regularized magnetic field as a function of the spectral index.

at the right). The nominal value of the first correlation peak (appearing in the title of the plot) is the one stemming from the three year best fit to the WMAP data alone.

In Section 4 we pointed out that a slight increase in the CDM fraction could be compensated by the presence of a magnetic field. This kind of potential degeneracies can only be thoroughly discussed in the framework of a general parameter estimation which also includes, to begin with, the magnetic field parameters. This analysis is beyond the scope of this paper, however, it is useful to investigate in an eclectic perspective, also other potentially interesting degeneracies which can be only assessed (or even partially resolved) in more systematic approaches.

One of these potential degeneracies involves the optical depth to reionization, i.e. τ . The increase of τ in a model without magnetic field yields a lower height of the Doppler peak. The values of the best fit model for WMAP data alone are used (see Eq. (4.1)) apart from the optical depth τ which is assumed to be varying between 0.09 and 0.105. In Figure 12 the height of the first acoustic peak is shown for different values of the magnetic spectral index n_B for different values of the magnetic field strength and of the optical depth τ .

The dependence on the magnetic spectral index becomes more important as B_L increases. While for $B_L = 2$ nG the height of the acoustic peak is basically independent of the spectral index, there is, for $B_L = 16$ nG, a nontrivial functional relation between the height of the peak and the magnetic spectral index. The variations in τ can be partially compensated by the addition of the magnetic field. Note, indeed, that the full line denote the experimental indetermination in the position of the peak.

In the near future the Planck explorer mission with its low frequency and high frequency instruments will be able to probe with higher accuracy the temperature autocorrelations, the polarization autocorrelations and cross-correlations. At the moment the putative Planck sensitivity can only be inferred from the last version of the Planck blue book [22]. The nominal sensitivity might not be the one effectively achieved by the instruments. Given the present specifications of the instruments, is not

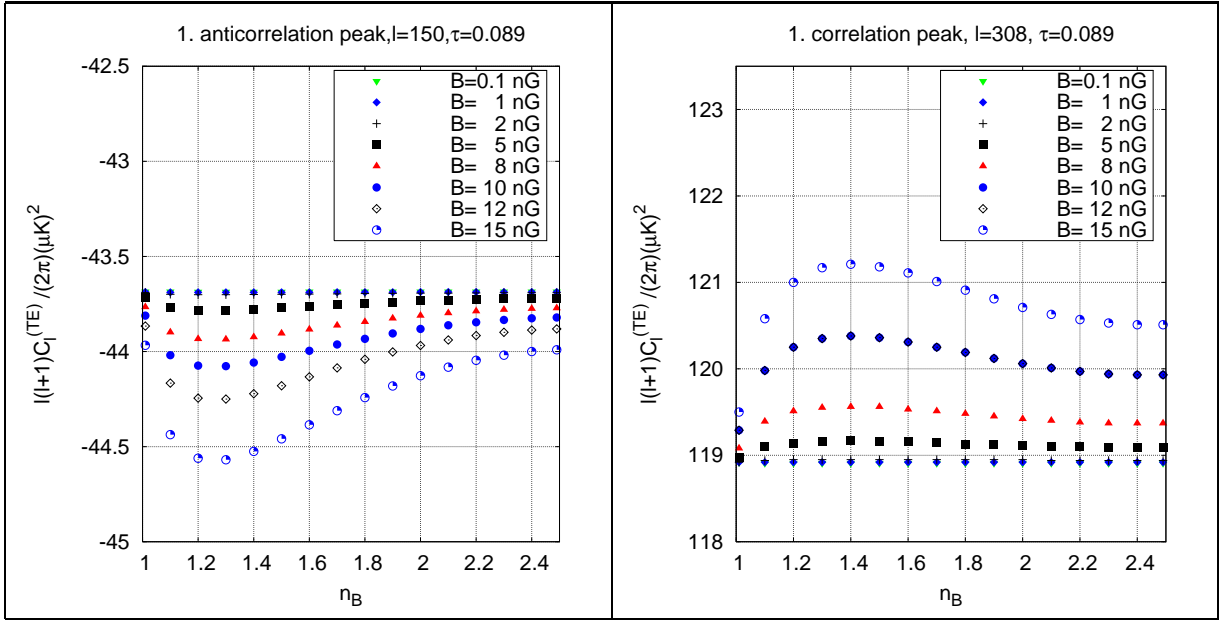


Figure 11: The height of the first anticorrelation and correlation peaks is illustrated, respectively, in the left and in the right plots.

clear in our case what are the best frequency channels to be combined in order to be mostly sensitive to the features introduced in the angular power spectra by the large-scale magnetic fields. In spite of this we find it interesting to elaborate on the possible implications of our endeavors for the Planck measurements at high multipoles (i.e. $\ell > 1500$).

To compare the nominal Planck sensitivity with the situation where magnetic fields are consistently included in a Λ CDM paradigm (with no tensors) we find it useful to adopt the following measure:

$$\mathcal{D}_{B,0}^{(TT)} \equiv \frac{|C_\ell^{(TT)}(B_L, n_B) - C_\ell^{(TT)}(B_L = 0)|}{C_\ell^{(TT)}(B_L = 0)}. \quad (6.1)$$

In Eq. (6.1) $C_\ell^{(TT)}(B_L = 0)$ is computed from the three year best fit to the WMAP data alone; $C_\ell^{(TT)}(B_L, n_B)$ is the TT correlation but computed with a magnetic field of regularized intensity B_L and characterized by a spectral index n_B . In different frameworks a similar estimator has been also employed [23, 24].

In Fig. 13 the quantity defined in Eq. (6.1) is illustrated for different values of the magnetic field intensity and of the spectral index. Note that $\mathcal{D}_{B,0}^{(TT)}$ estimates the difference induced by the presence of the magnetic field on the extrapolated three year WMAP best fit which can be used to deduce the nominal sensitivity of Planck for different regions in the multipole space. Adopting the three year WMAP best fit as fiducial model, the $1\text{-}\sigma$ errors can be inferred following the standard analysis also thoroughly reviewed in the Planck blue book (see [22])

$$(\Delta C_\ell^{(TT)})^2 = \frac{2}{(2\ell + 1)f_{\text{sky}}} \left(C_\ell + w_T^{-1} W_\ell^{-2} \right)^2, \quad (6.2)$$

$$w_T W_\ell^2 = \sum_c w_T^{(c)} e^{-\ell(\ell+1)/\ell_{\text{beam}}^c}. \quad (6.3)$$

In Eqs. (6.2)–(6.3) various assumptions should be made as far as the sky coverage and the relevant frequency channels are concerned. For this reason what we are presenting here are just preliminary

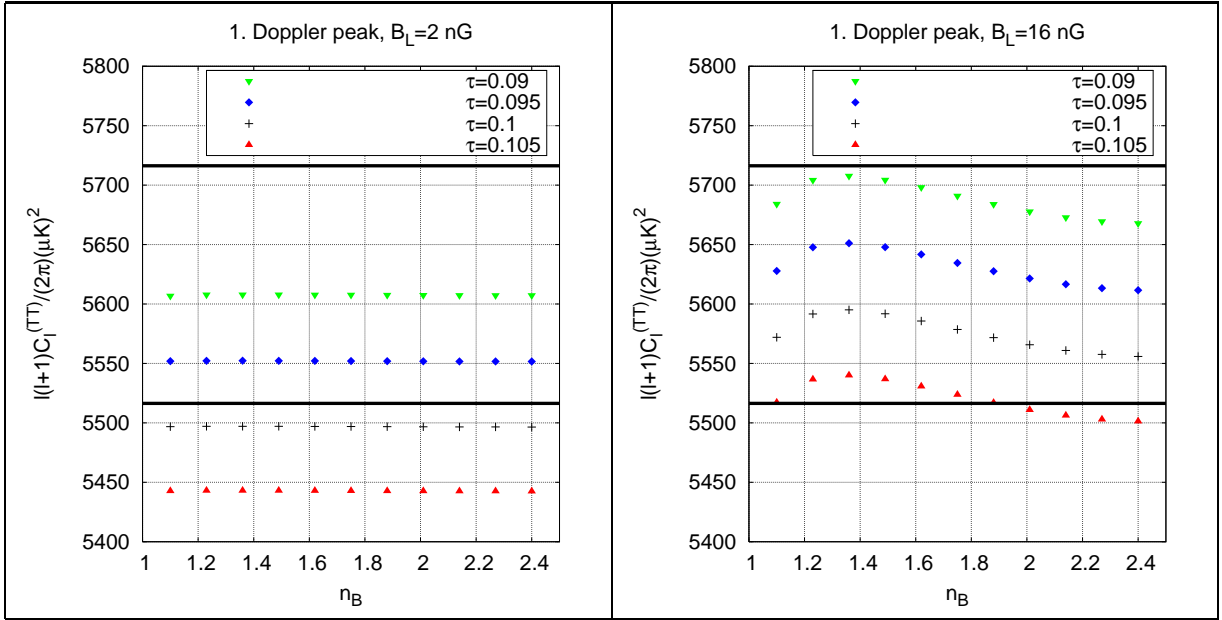


Figure 12: The height of the Doppler peak is presented as a function of the magnetic spectral index n_B for different values of the magnetic field strength and the optical depth. The horizontal lines indicate the observational bounds on the Doppler peak from WMAP3.

indications of what could be the trend of the Planck accuracy on the basis of the figures customarily employed by the Planck team [22]. Needless to say that the present estimate can be made more realistic once the effective Planck sensitivity will be available. Thus, it will be assumed that $f_{\text{sky}} \simeq 0.65$ corresponding to $\pm 20^\circ$ galactic cut. Furthermore the three lowest frequency channels of the high frequency instrument (i.e. 100 GHz, 143 GHz and 217 GHz) are combined and the sum appearing in Eq. (6.3) then extends over these three channels. To make explicit the sum it should be noted that $w_T^c = (\sigma_{\text{PT}}^c \vartheta_{\text{FWHM}}^c)^{-2}$ is the sensitivity per resolution element $\vartheta_{\text{FWHM}}^c \times \vartheta_{\text{FWHM}}^c$. The quantities σ_{PT}^c and $\vartheta_{\text{FWHM}}^c$ change for each of the three aforementioned channels. For σ_{PT}^c and $\vartheta_{\text{FWHM}}^c$ the values reported in the Planck blue book [22] have been selected. With these specifications in mind, the last quantity to be defined is $\ell_{\text{beam}}^c = \sqrt{8 \ln 2} / \theta_{\text{FWHM}}^c$ which measures the resolution of the Gaussian beam.

In Fig. 13 with the full curve the 1- σ error is reported. If the estimator leads to a value which is larger than the foreseen sensitivity it will be possible to make observational distinction between the magnetized model and the extrapolated three year best fit. In spite of the intrinsic uncertainty on the actual sensitivities of the instrument Fig. 13 is eloquent enough and then offers encouraging prospects for the region of high multipoles.

7 Concluding remarks

Large-scale magnetic fields are an observed component of the present Universe. Why are they present at the μG level in galaxies with different morphologies and different evolutionary histories? Why are they present inside rich clusters? When did they originate? Are they a cosmic relic in the same way as the adiabatic mode of curvature perturbations has a primeval origin?

It is difficult to answer these rather motivated questions just by building new models or by empha-

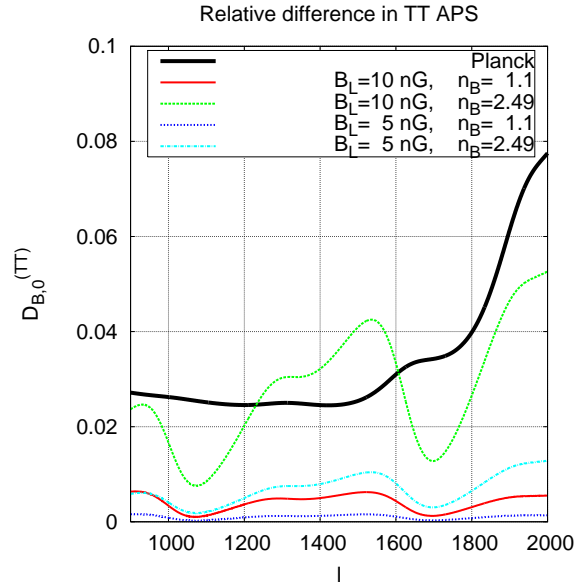


Figure 13: The estimator of Eq. (6.1) is illustrated in combination with the foreseen Planck sensitivity (full curve).

sizing single (potentially interesting) effects. It is even more difficult to run complicated simulations trying to reproduce large-scale magnetic fields without knowing the initial conditions to be imposed at early times, i.e. after decoupling. What we need is a systematic scrutiny of pre-decoupling physics to answer more modest but necessary questions. The most urgent one concerns the effect of large-scale magnetic fields on CMB observables. The combined numerical and analytical tools presented in this paper are a promising step along this direction. Needless to say that we plan to scrutinize more deeply all the manifold and exciting implications of our approach.

Acknowledgments

K. E. Kunze acknowledges the support of the “Ramón y Cajal” program as well as the grants FPA2005-04823 and FIS2006-05319 of the Spanish Science Ministry.

A From synchronous to longitudinal gauges

The treatment employed in the present analysis is the one stemming from the synchronous gauge description. We cross-checked all our results within the longitudinal approach. This cross-check is, under certain circumstances, mandatory. Indeed, in the synchronous gauge the freedom of selecting the coordinate system is not completely fixed. It is therefore important to have at hand a gauge description where the gauge parameters are completely fixed.

The strategy we followed has been often to derive the same quantity in the two different gauges and then compare the results by transforming the obtained expressions from one gauge to the other. For the effectiveness of this approach the longitudinal gauge is not essential. Rather we should say that the only essential requirement is a gauge where the freedom of selecting the coordinate system is completely fixed. So, for instance, the uniform curvature gauge would work equally well for this purpose [81, 82].

In the longitudinal gauge the metric of Eq. (2.1) is perturbed in such a way that non-vanishing entries of the first-order metric are

$$\delta_s g_{00} = 2a^2(\tau)\phi(k, \tau), \quad \delta_s g_{ij} = 2a^2(\tau)\psi(k, \tau)\delta_{ij}. \quad (\text{A.1})$$

The difference between the longitudinal and the synchronous coordinate systems is evident by comparing Eq. (A.1) with Eq. (2.7). Following standard techniques we can find the precise relation between the longitudinal and the synchronous degrees of freedom:

$$\begin{aligned} \phi(k, \tau) &= -\frac{1}{2k^2} \{ [h(k, \tau) + 6\xi(k, \tau)]'' + \mathcal{H}[h(k, \tau) + 6\xi(k, \tau)]' \}, \\ \psi(k, \tau) &= -\xi(k, \tau) + \frac{\mathcal{H}}{2k^2} [h(k, \tau) + 6\xi(k, \tau)]', \\ \bar{\delta}(k, \tau) &= \delta(k, \tau) + \frac{3\mathcal{H}(w+1)}{2k^2} [h(k, \tau) + 6\xi(k, \tau)]' \\ \bar{\theta}(k, \tau) &= \theta(k, \tau) - \frac{1}{2} [h(k, \tau) + 6\xi(k, \tau)]'. \end{aligned} \quad (\text{A.2})$$

The barred quantities (i.e. $\bar{\delta}$ and $\bar{\theta}$) are defined in the longitudinal gauge and w is the barotropic index of the corresponding species. Similarly the transformation for θ holds for a generic peculiar velocity. The inverse transformations can be also obtained and they are:

$$\begin{aligned} \xi(k, \tau) &= -\psi(k, \tau) - \frac{\mathcal{H}}{a} \int^\tau a(\tau')\phi(k, \tau')d\tau', \\ h(k, \tau) &= 6\psi(k, \tau) + 6\frac{\mathcal{H}}{a} \int^\tau a(\tau')\phi(k, \tau')d\tau' - 2k^2 \int^\tau \frac{d\tau'}{a(\tau')} \int^{\tau'} a(\tau'')\phi(k, \tau'')d\tau'', \\ \delta(k, \tau) &= \bar{\delta}(k, \tau) + \frac{3\mathcal{H}(w+1)}{a} \int^\tau a(\tau')\phi(k, \tau')d\tau' \\ \theta(k, \tau) &= \bar{\theta}(k, \tau) - \frac{k^2}{a} \int^\tau a(\tau')\phi(k, \tau')d\tau'. \end{aligned} \quad (\text{A.3})$$

The integrals appearing in Eq. (A.3) for the expressions of θ and h imply two integration constants which can be space dependent and which are fixed by demanding that $\theta_c = 0$ and that h has no constant mode.

The solution for the magnetized adiabatic mode will be, in the longitudinal gauge,

$$\begin{aligned}
\phi_*(k) &= \frac{20C(k)}{4R_\nu + 15} - 2\frac{R_\gamma[4\sigma_B(k) - R_\nu\Omega_B(k)]}{4R_\nu + 15}, \\
\psi_*(k) &= \left(\frac{8R_\nu + 20}{4R_\nu + 15}\right)C(k) + \frac{R_\gamma[4\sigma_B(k, \tau) - R_\nu\Omega_B(k)]}{4R_\nu + 15}, \\
\psi_*(k) &= \left(1 + \frac{2}{5}R_\nu\right)\phi_*(k) + \frac{R_\gamma}{5}[4\sigma_B(k) - R_\nu\Omega_B(k)], \\
\delta_\gamma(k, \tau) &= -2\phi_*(k) - R_\gamma\Omega_B(k), \\
\delta_\nu(k) &= -2\phi_*(k) - R_\gamma\Omega_B(k), \\
\delta_c(k) &= -\frac{3}{2}\phi_*(k) - \frac{3}{4}R_\gamma\Omega_B(k), \\
\delta_b(k) &= -\frac{3}{2}\phi_*(k) - \frac{3}{4}R_\gamma\Omega_B(k), \\
\sigma_\nu(k, \tau) &= -\frac{R_\gamma}{R_\nu}\sigma_B(k) + \frac{k^2\tau^2}{6R_\nu}[\psi_*(k) - \phi_*(k)], \\
\theta_{\gamma b}(k, \tau) &= \frac{k^2\tau}{2}\left[\phi_*(k) + \frac{R_\nu\Omega_B(k)}{2} - 2\sigma_B(k)\right], \\
\theta_\nu(k, \tau) &= \frac{k^2\tau}{2}\left[\phi_*(k) - \frac{R_\gamma\Omega_B(k)}{2} + 2\frac{R_\gamma}{R_\nu}\sigma_B(k)\right], \\
\theta_c(k, \tau) &= \frac{k^2\tau}{2}\phi_*(k). \tag{A.4}
\end{aligned}$$

It can be easily checked that the solution (A.5) is a solution of the full system written in the longitudinal frame.

There is an important point to be borne in mind when setting initial conditions. We set initial conditions deep in the radiation epoch. Now, the constant $C = C(k)$ that appears in the synchronous description can be actually related with curvature perturbations on comoving orthogonal hypersurfaces \mathcal{R} . In the longitudinal gauge we do know that, deep in the radiation epoch,

$$\mathcal{R}(k) = -\psi - \frac{\mathcal{H}\phi + \psi'}{\mathcal{H}^2 - \mathcal{H}'} \simeq -\psi_*(k) - \frac{\phi_*(k)}{2} = -2C(k) \tag{A.5}$$

In the longitudinal gauge we can also easily express the variable ζ introduced in Eq. (2.73). In terms of the longitudinal degrees of freedom

$$\zeta = -\psi - \frac{\delta^L\rho_t + \delta\rho_B}{\rho'_t}, \tag{A.6}$$

where $\delta^L\rho_t$ is the total density fluctuation in the longitudinal gauge. In the longitudinal gauge the Hamiltonian constraint reads

$$\nabla^2\phi - 3\mathcal{H}(\mathcal{H}\phi + \psi') = 4\pi Ga^2(\delta^L\rho_t + \delta\rho_B). \tag{A.7}$$

Using Eqs. (A.5) and (A.6) into Eq. (A.7) the Hamiltonian constraint can be written as

$$\zeta = \mathcal{R} + \frac{\nabla^2\psi}{12\pi Ga^2(\rho_t + p_t)} \tag{A.8}$$

where Eqs. (2.3) and (2.4) have been used. Equation (A.8) has been quoted and independently obtained in Eq. (2.75)

References

- [1] W. A. Hiltner, *Science* **109**, 165 (1949).
- [2] J. S. Hall, *Science* **109**, 166 (1949).
- [3] L. J. Davis J. L. Greenstein: *Astrophys. J.* **114**, 206 (1951).
- [4] H. Alfvén, *Arkiv. Mat. F. Astr., o. Fys.* **29 B**, 2 (1943).
- [5] L. Spitzer, *Physics of Fully ionized plasmas* (J. Wiley and Sons, New York, 1962).
- [6] N. A. Krall, A. W. Trivelpiece: *Principles of Plasma Physics*, (San Francisco Press, San Francisco 1986).
- [7] D. Biskamp, *Non-linear Magnetohydrodynamics* (Cambridge University Press, Cambridge, 1994).
- [8] T. J. M Boyd, J. J. Serson: *The physics of plasmas*, (Cambridge University Press, Cambridge, UK, 2003).
- [9] Ya. B. Zeldovich, A. A. Ruzmaikin, and D.D. Sokoloff, *Magnetic Fields in Astrophysics* (Gordon and Breach Science, New York, 1983); M. Giovannini, *Int. J. Mod. Phys. D* **13**, 391 (2004); A. Brandenburg and K. Subramanian, *Phys. Rep.* **417** 1 (2005).
- [10] A. A. Ruzmaikin, A. M. Shukurov, D. D. Sokoloff *Magnetic Fields of Galaxies*, (Kluwer Academic Publisher, Dordrecht, 1988); E. Zweibel and C. Heiles, *Nature***385**, 131 (1997).
- [11] D. N. Spergel *et al.* [WMAP Collaboration], *Astrophys. J. Suppl.* **170**, 377 (2007).
- [12] L. Page *et al.* [WMAP Collaboration], *Astrophys. J. Suppl.* **170**, 335 (2007).
- [13] H. V. Peiris *et al.* [WMAP Collaboration], *Astrophys. J. Suppl.* **148**, 213 (2003).
- [14] D. N. Spergel *et al.* [WMAP Collaboration], *Astrophys. J. Suppl.* **148**, 175 (2003).
- [15] C. L. Bennett *et al.* [WMAP Collaboration], *Astrophys. J. Suppl.* **148**, 1 (2003).
- [16] T. E. Montroy *et al.*, *Astrophys. J.* **647**, 813 (2006); C. I. Kuo *et al.* [ACBAR collaboration], *Astrophys. J.* **600**, 32 (2004). A. C. S. Readhead *et al.*, *Astrophys. J.* **609**, 498 (2004); C. Dickinson *et al.*, *Mon. Not. Roy. Astron. Soc.* **353**, 732 (2004).
- [17] W. L. Freedman *et al.*, *Astrophys. J.* **553**, 47 (2001); S. Cole *et al.* [The 2dFGRS Collaboration], *Mon. Not. Roy. Astron. Soc.* **362** , 505 (2005);
- [18] D. J. Eisenstein *et al.* [SDSS Collaboration], *Astrophys. J.* **633**, 560 (2005); M. Tegmark *et al.* [SDSS Collaboration], *Astrophys. J.* **606**, 702 (2004).
- [19] P. Astier *et al.* [The SNLS Collaboration], *Astron. Astrophys.* **447**, 31 (2006).
- [20] A. G. Riess *et al.* [Supernova Search Team Collaboration], *Astrophys. J.* **607**, 665 (2004); B. J. Barris *et al.*, *Astrophys. J.* **602**, 571 (2004).
- [21] E. Semboloni *et al.*, arXiv:astro-ph/0511090; H. Hoekstra *et al.*, *Astrophys. J.* **647**, 116 (2006).

- [22] See, for instance, <http://www.rssd.esa.int/index.php?project=PLANCK>.
- [23] M. Zaldarriaga and U. Seljak, Phys. Rev. D **58**, 023003 (1998); W. H. Kinney, Phys. Rev. D **58**, 123506 (1998).
- [24] P. Naselsky and L. Y. Chiang, Mon. Not. Roy. Astron. Soc. **347**, 795 (2004).
- [25] M. Giovannini and K. E. Kunze, *A magnetized completion of the LambdaCDM paradigm*, arXiv:0712.1977[astro-ph].
- [26] Ya. Zeldovich, *Sov. Phys. JETP***21**, 656 (1965).
- [27] E. Harrison, Phys. Rev. Lett. **18**, 1011 (1967); Mon. Not. R. Astr. Soc. **147**, 279 (1970).
- [28] J. Barrow, K. Subramanian: Phys. Rev. Lett. **81**, 3575 (1998); J. Barrow, K. Subramanian: Phys. Rev. D **58**, 83502 (1998); K. Subramanian, T. Seshadri, and J. Barrow, Mon. Not. Roy. Astron. Soc. **344**, L31 (2003).
- [29] C. Tsagas, R. Maartens: Phys. Rev. D **61**, 083519 (2000); A. Mack, T. Kahniashvili, A. Kosowsky: Phys. Rev. D **65**, 123004 (2002); A. Lewis, Phys. Rev. D **70**, 043518 (2004); T. Kahniashvili, B. Ratra, Phys. Rev. D **71**, 103006 (2005).
- [30] M. Giovannini, Class. Quant. Grav. **23**, R1 (2006).
- [31] M. Giovannini, Phys. Rev. D **73**, 101302 (2006).
- [32] M. Giovannini, Phys. Rev. D **74**, 063002 (2006); M. Giovannini, Class. Quant. Grav. **23**, 4991 (2006).
- [33] M. Giovannini, PMC Phys. A **1**, 5 (2007); Phys. Rev. D **76**, 103508 (2007)
- [34] E. Bertschinger, *COSMICS: Cosmological Initial Conditions and Microwave Anisotropy Codes* arXiv:astro-ph/9506070.
- [35] C. P. Ma and E. Bertschinger, Astrophys. J. **455**, 7 (1995)
- [36] U. Seljak and M. Zaldarriaga, Astrophys. J. **469**, 437 (1996).
- [37] M. Zaldarriaga, D. N. Spergel and U. Seljak, Astrophys. J. **488**, 1 (1997).
- [38] W. Press and E. Vishniac, Astrophys. J. **239**, 1 (1980); Astrophys. J. **236**, 323 (1980).
- [39] J. M. Bardeen, Phys. Rev. D **22**, 1882 (1980).
- [40] S. Weinberg, Phys. Rev. D **67**, 123504 (2003).
- [41] E. M. Lifshitz and I. M. Khalatnikov, Sov. Phys. Usp. **6**, 495 (1964) [*Usp. Fiz. Nauk.* **80**, 391 (1964)].
- [42] G.F.R. Ellis and M. Bruni, Phys. Rev. D **40**, 1804 (1989); M. Bruni, G. F. R. Ellis and P. K. S. Dunsby, Class. Quantum Grav. **9**, 921 (1992).
- [43] C. G. Tsagas and J. D. Barrow, Class. Quant. Grav. **14**, 2539 (1997); *ibid.* **15**, 3523 (1998).

- [44] M. Giovannini, Phys. Rev. D **61**, 063502 (2000); Phys. Rev. D **61**, 063004 (2000); T. Kahniashvili and B. Ratra, Phys. Rev. D **71**, 103006 (2005); K. Bamba, Phys. Rev. D **74**, 123504 (2006); K. Bamba, C. Q. Geng and S. H. Ho, arXiv:0712.1523 [hep-ph].
- [45] H. Kodama and M. Sasaki, Prog. Theor. Phys. Suppl. **78**, 1 (1984).
- [46] K. A. Malik and D. Wands, JCAP **0502**, 007 (2005).
- [47] M. Giovannini, Class. Quant. Grav. **22**, 5243 (2005); Phys. Lett. B **622**, 349 (2005).
- [48] M. Abramowitz and I. A. Stegun, *Handbook of Mathematical Functions* (Dover, New York, 1972).
- [49] I. S. Gradshteyn and I. M. Ryzhik, *Tables of Integrals, Series and Products (fifth edition)*, (Academic Press, New York, 1994).
- [50] M. Giovannini and K. Kunze, work in progress.
- [51] K. Enqvist and H. Kurki-Suonio, Phys. Rev. D **61**, 043002 (2000).
- [52] M. Zaldarriaga and D. D. Harari, Phys. Rev. D **52**, 3276 (1995).
- [53] P. J. E. Peebles and J. T. Yu, Astrophys. J. **162** 815 (1970).
- [54] H. Jorgensen, E. Kotok, P. Naselsky, and I Novikov, Astron. Astrophys. **294**, 639 (1995).
- [55] P. Naselsky and I. Novikov, Astrophys. J. **413**, 14 (1993).
- [56] U. Seljak, Astrophys. J. **435**, L87 (1994).
- [57] W. Hu and N. Sugiyama, Astrophys. J. **444**, 489 (1995).
- [58] K. E. Kunze, Phys. Lett. B **623**, 1 (2005).
- [59] J. L. Han, K. Ferriere, R. N. Manchester, Astrophys. J. **610**, 820 (2004).
- [60] O. Goldshmidt and Y. Rephaeli, Astrophys. J. **411**, 518 (1993).
- [61] A. Crusius-Wätzel, P. Biermann, R. Schlickeiser, and I. Lerche, Astrophys. J. **360**, 417 (1990).
- [62] See, for instance, <http://www.skatelescope.org>.
- [63] B.M. Gaensler, R. Beck, L. Feretti, New Astron. Rev. **48**, 1003 (2004).
- [64] R. Beck, Astron.Nachr. **327**, 512 (2006).
- [65] R. Beck, A. Brandenburg, D. Moss, A. Skhurov, D. Sokoloff Annu. Rev. Astron. Astrophys. **34**, 155 (1996).
- [66] D. Boyanovsky, H. J. de Vega and N. G. Sanchez, Phys. Rev. D **74**, 123006 (2006).
- [67] D. Boyanovsky, H. J. de Vega and N. G. Sanchez, Phys. Rev. D **74**, 123007 (2006).
- [68] K. Enqvist, H. Kurki-Suonio and J. Valiviita, Phys. Rev. D **62**, 103003 (2000).
- [69] H. Kurki-Suonio, V. Muhonen and J. Valiviita, Phys. Rev. D **71**, 063005 (2005).

- [70] J. Valiviita and V. Muhonen, Phys. Rev. Lett. **91**, 131302 (2003).
- [71] R. Keskitalo, H. Kurki-Suonio, V. Muhonen and J. Valiviita, JCAP **0709**, 008 (2007).
- [72] E. M. Leitch *et al.*, Astrophys. J. **624**, 10 (2005).
- [73] D. Barkats *et al.*, Astrophys. J. **619**, L127 (2005).
- [74] A. C. S. Readhead *et al.*, arXiv:astro-ph/0409569.
- [75] P. Ade *et al.* [QUaD Collaboration], arXiv:0705.2359 [astro-ph].
- [76] A. Kosowsky and A. Loeb, Astrophys. J. **469**, 1 (1996); D. D. Harari, J. D. Hayward and M. Zaldarriaga, Phys. Rev. D **55**, 1841 (1997); M. Giovannini, Phys. Rev. D **56**, 3198 (1997).
- [77] C. Scoccola, D. Harari and S. Mollerach, Phys. Rev. D **70**, 063003 (2004).
- [78] A. Kosowsky, T. Kahniashvili, G. Lavrelashvili and B. Ratra, Phys. Rev. D **71**, 043006 (2005).
- [79] L. Campanelli, A. D. Dolgov, M. Giannotti and F. L. Villante, Astrophys. J. **616**, 1 (2004).
- [80] M. Giovannini, Phys. Rev. D **71**, 021301 (2005).
- [81] J. Hwang, Astrophys. J. **375**, 443 (1990).
- [82] J. Hwang and H. Noh, Class. Quant. Grav. **19**, 527 (2002).